

COSMOGLOBE DR2. III. Improved modeling of zodiacal light with COBE-DIRBE through global Bayesian analysis

M. San^{1*}, A. Bonato^{2**}, M. Galloway¹, E. Gjerløw¹, D. J. Watts¹, R. Aurvik¹, A. Basyrov¹, L. A. Bianchi¹, M. Brilenkov¹, H. K. Eriksen¹, U. Fuskeland¹, K. A. Glasscock¹, L. T. Hergt³, D. Herman¹, J. G. S. Lunde¹, A. I. Silva Martins¹, D. Sponseller⁴, N.-O. Stutzer¹, R. M. Sullivan¹, H. Thommesen¹, V. Vikenes¹, I. K. Wehus¹, and L. Zapelli^{2,6,5}

¹ Institute of Theoretical Astrophysics, University of Oslo, Blindern, Oslo, Norway

² Dipartimento di Fisica, Università degli Studi di Milano, Via Celoria, 16, Milano, Italy

³ Laboratoire de Physique des 2 infinis – Irène Joliot Curie (IJCLab), Orsay, France

⁴ Department of Space, Earth and Environment, Chalmers University of Technology, Gothenburg, Sweden

⁵ Università di Trento, Università degli Studi di Milano, CUP E66E23000110001

⁶ INFN sezione di Milano, 20133 Milano, Italy

January 12, 2026

ABSTRACT

We present an improved zodiacal light (ZL) model for *COBE*-DIRBE derived through global Bayesian analysis within the COSMOGLOBE Data Release 2 (DR2) framework. The parametric form of the ZL model is inspired by that introduced by Kelsall et al. (1998), but the specific best-fit parameter values are re-derived using the combination of DIRBE Calibrated Individual Observations (CIO), *Planck* HFI sky maps, and WISE and *Gaia* compact object catalogs. Furthermore, the ZL parameters are fitted jointly with astrophysical parameters, such as thermal dust and starlight emission, and the new model takes into account excess radiation that appears stationary in solar-centric coordinates as reported in a companion paper. The relative differences between the predicted signals from K98 and our new model are $\lesssim 3\%$ in the 12 and 25 μm channels over the full sky. The zero-levels of the cleaned DR2 maps are lower than those of the K98 Zodiaca light Subtracted Mission Average (ZSMA) maps by $\sim 30 \text{ kJy/sr}$ at $1.25\text{--}3.5 \mu\text{m}$, which is larger than the entire predicted contribution from high-redshift galaxies to the Cosmic Infrared Background (CIB) at the same wavelengths. At high Galactic latitudes the total RMS of each DR2 map is lower than the corresponding DIRBE ZSMA map of $\sim 30\%$ at wavelengths up to and including $3.5 \mu\text{m}$, and $\sim 80\%$ at wavelengths $4.9\text{--}25 \mu\text{m}$. The cleaned DR2 maps at 4.9 and $12 \mu\text{m}$ are now, for the first time, visually dominated by Galactic signal at high latitudes rather than by ZL residuals. Even the $100 \mu\text{m}$ channel, which has served as a cornerstone for Galactic studies for three decades, appears cleaner in the current processing. Still, obvious ZL residuals can be seen in several of the DR2 maps, and further work is required to mitigate these. Joint analysis with existing and future high-resolution full-sky surveys such as *AKARI*, *IRAS*, *Planck* HFI, and SPHEREx will be essential both to break key degeneracies in the current model and to determine whether the reported solar-centric excess radiation has a ZL or instrumental origin. On the algorithmic side, more efficient methods for probing massively multi-peaked likelihoods should be explored and implemented. Thus, while the results presented in this paper do redefine the state-of-the-art for DIRBE modeling, it also only represents the first among many steps toward a future optimal Bayesian ZL model.

Key words. Zodiacal dust, Interplanetary medium, Cosmology: cosmic background radiation

1 Contents

2 1 Introduction

2 2 Zodiacal light modeling

| | | |
|-----|---|---|
| 2.1 | Parameterization of interplanetary dust | 2 |
| 2.2 | Zodiacal components | 3 |
| 2.3 | Radiative and scattering properties | 3 |
| 2.4 | Model intuition | 4 |
| 2.5 | Numerical optimizations | 5 |

3 Methods

| | | |
|-----|--|---|
| 3.1 | Data model, posterior distribution, and Gibbs sampling | 5 |
| 3.2 | Comparison with K98 fitting algorithm | 6 |
| 3.3 | Posterior sampling by non-linear optimization | 8 |

4 Data

| | | | | |
|---|-----|--|----|----|
| 2 | 4.1 | DIRBE Calibrated Individual Observations | 10 | 15 |
| 2 | 4.2 | Masks | 11 | 16 |

5 Results

| | | | | |
|---|-----|-----------------------------------|----|----|
| 5 | 5.1 | Markov chains | 11 | 18 |
| 5 | 5.2 | Updated ZL model | 13 | 19 |
| 5 | 5.3 | Goodness-of-fit | 14 | 20 |
| 5 | 5.4 | Comparison of ZSMA maps | 18 | 21 |

6 Conclusions

| | | | | |
|---|---|--|----|----|
| 6 | A | Component-wise zodiacal light maps and number density cross-sections | 23 | 24 |
|---|---|--|----|----|

B Interplanetary dust parameter atlas

* Corresponding author: M. San; metin.san@astro.uio.no

** Corresponding author: A. Bonato; angela.bonato1@studenti.unimi.it

26 1. Introduction

27 Zodiacal light (ZL, sometimes zodiacal emission or interplane-
 28 tary dust emission) is the primary source of diffuse radiation ob-
 29 served in the infrared sky between 1–100 μm (see, e.g., Leinert
 30 et al. 1998a and references therein). This radiation comes from
 31 scattering and re-emission of sunlight from interplanetary dust
 32 (IPD) grains, and was first mapped in detail by the *IRAS* satellite
 33 (Neugebauer et al. 1984).

34 The inner Solar system is embedded in a Sun centered cloud
 35 of IPD, with a symmetry axis tilted slightly with respect to the
 36 Ecliptic, known as the zodiacal cloud. The ZL is seasonal, and
 37 its appearance in the sky changes as the Earth moves through
 38 the IPD distribution. The most common way to model the ob-
 39 server position-dependent ZL is to evaluate a line-of-sight inte-
 40 gral for each observation directly in the time-ordered domain.
 41 The time-varying and three-dimensional nature of the ZL makes
 42 it one of the most challenging foregrounds to model in astrophys-
 43 ical and cosmological studies of the infrared sky. The lack of a
 44 high-accuracy ZL model has left a large part of the electromag-
 45 netic spectrum inaccessible to cosmological analysis attempting
 46 to measure the Cosmic Infrared Background (CIB; Partridge &
 47 Peebles 1967; Hauser et al. 1998; Hauser & Dwek 2001).

48 One of the most widely used ZL models in the field of cos-
 49 mology is the *COBE*-DIRBE model by Kelsall et al. (1998), of-
 50 ten simply referred to as the K98 model. This is a parametric
 51 model that describes the three-dimensional distribution and ra-
 52 diative properties of IPD using time-dependent measurements
 53 from the *COBE*-DIRBE instrument (Hauser et al. 1998). There
 54 have been extensions to this model proposed since this origi-
 55 nal work, primarily to explain residual monopoles seen in com-
 56 parisons to other data (Sano et al. 2020; Korngut et al. 2022;
 57 Carleton et al. 2022). Additionally, there have been several di-
 58 rect measurements of the IPD density (Poppe et al. 2019; Szalay
 59 et al. 2020), some of which suggest that the IPD densities may
 60 be greater than previously predicted (Nieto et al. 2005). Despite
 61 these potential shortcomings, the Kelsall model remains the de-
 62 facto model in the CMB field today.

63 Since the DIRBE experiment, our understanding of the in-
 64 frared sky has improved with new observational data from exper-
 65 iments like WISE (Wright et al. 2010), *Planck* HFI (Planck Col-
 66 laboration III 2020), and *Gaia* (Gaia Collaboration et al. 2016).
 67 However, these experiments have largely been analyzed indi-
 68 videntally, and little or no coordinated effort has been made to-
 69 ward combining the data from these experiments into one over-
 70 all state-of-the-art model of the infrared sky. The main goal of
 71 the current work, summarized in a series of papers collectively
 72 denoted COSMOGLOBE Data Release 2, is to make the first step
 73 toward such a concordance model by leveraging recent compu-
 74 tational advances in Bayesian cosmological data analysis by
 75 the BEYONDPLANCK (BeyondPlanck Collaboration et al. 2023;
 76 Galloway et al. 2023, and references therein) and COSMOGLOBE
 77 (Watts et al. 2023) collaborations. The computer code implemen-
 78 tation is called Commander3 (Galloway et al. 2023), which is a
 79 Bayesian Gibbs sampler that was originally designed for end-to-
 80 end analysis of cosmic microwave background (CMB) experi-
 81 ments, in particular *Planck* LFI (Planck Collaboration II 2020)
 82 and *WMAP* (Bennett et al. 2013). However, as demonstrated in
 83 the current work, the same algorithms are, after relatively minor
 84 modifications, directly applicable to infrared measurements.

85 One of the most important generalizations required for appli-
 86 cation of Commander3 to the infrared sky is the implementa-
 87 tion of an accurate ZL model to remove the time-varying ZL. In this
 88 paper we therefore implement in Commander3 support for the

K98 model combined with the scattering phase function de-
scribed by Hong (1985), and we apply this to the time-domain
 DIRBE data. This new code implementation is based on ZodiPy
 (San 2024), which is an Astropy-affiliated Python package for
 ZL simulations.¹ As an early application of this framework, San
 et al. (2022) demonstrated the removal of ZL from the DIRBE
 time-ordered data (TOD) with ZodiPy using the K98 model.

ZL is found to be polarized in the near-infrared in both the
 DIRBE and *CIBER* data (Takimoto et al. 2022, 2023). We make
 no attempts at modeling polarized ZL in this analysis, but a natu-
 ral next step in this analysis would be to include the polarization
 data from the 1.25, 2.2, and 3.5 μm DIRBE bands.

The rest of the paper is organized as follows. In Sect. 2,
we introduce our ZL model and discuss implementation and
 optimization aspects. Next, in Sect. 3, we describe the algo-
 rithms and methods used to fit the ZL parameters within the
 COSMOGLOBE framework. In Sect. 4, we describe the data used
 in the current analysis. Next, in Sect. 5, we present our updated
 ZL model and compare this with the K98 model. Finally, we
 conclude in Sect. 6.

2. Zodiacal light modeling

ZL is commonly modeled sample-by-sample in time-domain by
 performing line-of-sight integration at each observation through
 a parametric three-dimensional model of the IPD distribution.
We adopt a modified version of the general parametrization
as introduced by K98 for the current Commander3 implemen-
 tation, and in this section we briefly review the main aspects of
 this model, aiming to build intuition about the underlying para-
 metric model. We also consider a few numerical approximations
 that reduce the overall computational cost. For full details of this
 model, we refer the interested reader to Kelsall et al. (1998) and
 Hong (1985).

2.1. Parameterization of interplanetary dust

IPD in the zodiacal cloud is overall smooth and stable (Leinert & Pitz 1989), and most of the dust may be accounted for by a diffuse cloud-like component (Kelsall et al. 1998). The origin of IPD is debris mainly from comets (Liou et al. 1995; Ipatov et al. 2008; Rigley & Wyatt 2022), asteroids (Dermott et al. 1984) and meteoroids (Dikarev & Schwarz 2015), with potential additions from planets (Jorgensen et al. 2021), the Kuiper belt (Mann et al. 2009), and interstellar dust passing through the Solar system (Rowan-Robinson & May 2013). The relative contribution to the overall IPD density from these sources is not well known, but many models predict the main source to be low-eccentricity Jupiter family comets that rapidly disintegrate due to frequent trips through the inner Solar system. Within the mostly smooth zodiacal cloud, fine structures exist near the Ecliptic plane as a result of collisions and fragmentation in the asteroid belt and gravitational resonance and disturbance in the orbit of the planets (Low et al. 1984; Dermott et al. 1984, 1994; Reach et al. 1997). There are also structures found in the orbits of other solar system planets, (Kennedy et al. 2011; Jones et al. 2013; Stenborg et al. 2018), but these are potential extensions to the Kelsall model.

We model the IPD distribution as a combination of sev-
 eral zodiacal components, each described by a number density
 $n_c(x, y, z)$, where c indicates components and x , y and z indicate
 heliocentric Ecliptic coordinates. Each zodiacal component is al-
 lowed to have a heliocentric offset $(x_{0,c}, y_{0,c}, z_{0,c})$, such that the

¹ <https://cosmoglobe.github.io/zodipy/>

147 component-centric coordinates become

$$\begin{aligned} x_c &= x - x_{0,c} \\ y_c &= y - y_{0,c} \\ z_c &= z - z_{0,c}. \end{aligned} \quad (1)$$

148 Additionally, each zodiacal component is allowed to have a
149 plane of symmetry that is different from the Ecliptic, which is
150 defined by an inclination i_c and an ascending node Ω_c . Components
151 that happen to be azimuthally symmetric are then fully
152 described by a radial distance r_c from the origin and the height
153 above the symmetry plane Z_c :

$$r_c = \sqrt{x_c^2 + y_c^2 + z_c^2}, \quad (2)$$

$$Z_c = x_c \sin \Omega_c \sin i_c - y_c \cos \Omega_c \sin i_c + z_c \cos i_c, \quad (3)$$

$$\zeta_c = \frac{|Z_c|}{r_c}, \quad (4)$$

154 with ζ_c being the radial height above the symmetry plane.

155 2.2. Zodiacal components

156 With these definitions in hand, we now define parametric models
157 for each IPD component type.

158 2.2.1. Smooth cloud

159 By far the most important component is typically referred to as
160 the “zodiacal cloud”. This component represents the smooth IPD
161 distribution in the inner Solar system. Its number density is mod-
162 eled as

$$n_C(x, y, z) = n_{0,C} r_C^{-\alpha} f(\zeta_C), \quad (5)$$

163 where $n_{0,C}$ is the number density at 1 AU, α is a power-law ex-
164 ponent, $f(\zeta_C)$ is the fan-like vertical distribution given as

$$f(\zeta_C) = \exp[-\beta g(\zeta_C)^\gamma], \quad (6)$$

165 with

$$g(\zeta_C) = \begin{cases} \zeta_C^2 / 2\mu & \text{for } \zeta_C < \mu, \\ \zeta_C - \mu/2 & \text{for } \zeta_C \geq \mu, \end{cases} \quad (7)$$

166 where β , γ and μ are shape parameters.

167 2.2.2. Dust bands

168 Next, three dust bands are included in the model to represent
169 the observed shoulder-like structure in the *IRAS* scans across the
170 Ecliptic plane. These bands appear at Ecliptic latitudes of ap-
171 proximately $\pm 1.4^\circ$, $\pm 10^\circ$, and $\pm 15^\circ$, and are associated with a
172 blend of the Themis and Koronis, the Eos, and the Io/Maria as-
173 teroid families, respectively (Reach et al. 1997). Each dust band,
174 indicated by B_i , is modeled as

$$n_{B_i}(x, y, z) = \frac{3n_{0,B_i}}{r_{B_i}} \exp\left[-\left(\frac{\zeta_{B_i}}{\delta_{\zeta_{B_i}}}\right)^6\right] \left[1 + \left(\frac{\zeta_{B_i}}{\delta_{\zeta_{B_i}}}\right)^{p_i} v_i^{-1}\right] \quad (8)$$

$$\times \left\{1 - \exp\left[-\left(\frac{r_{B_i}}{\delta_{r_{B_i}}}\right)^{20}\right]\right\}, \quad (9)$$

175 where n_{0,B_i} is the number density of band B_i at 3 AU, $\delta_{r_{B_i}}$ is the
176 inner radial cut-off, and p_i , v_i and $\delta_{\zeta_{B_i}}$ are shape parameters.

2.2.3. Circumsolar ring and Earth-trailing feature

177

Finally, a circumsolar ring (denoted “SR”) component is in-
178 cluded in the model to represent dust that has accumulated in
179 Earth’s orbit due to gravitational effects (Dermott et al. 1994).
180 This component also includes an enhancement to the IPD dis-
181 tribution at Earth’s wake, known as the “Earth-trailing feature”
182 (denoted “TF”). The composite ring component (denoted “R”)
183 is then modeled as
184

$$n_R(x, y, z, \theta) = n_{0,SR} \exp\left[-\frac{(r_R - r_{0,SR})^2}{\sigma_{R,SR}^2} - \frac{|Z_R|}{\sigma_{Z,SR}}\right] \quad (10)$$

$$+ n_{0,TF} \exp\left[-\frac{(r_R - r_{0,TF})^2}{\sigma_{R,TF}^2} - \frac{|Z_F|}{\sigma_{Z,TF}} - \frac{(\theta - \theta_{0,TF})^2}{\sigma_{\theta,TF}^2}\right], \quad (11)$$

where θ is the heliocentric longitude of the Earth, and the radial
185 locations $r_{0,SR}$, $r_{0,TF}$ specify the distances to the peak densities
186 $n_{0,SR}$, $n_{0,TF}$. The σ parameters are length scales for the r , Z and θ
187 parameters, respectively. We note that the Earth-trailing feature
188 depends on the position of the Earth and does not have a plane
189 symmetry like the other zodiacal components.
190

2.3. Radiative and scattering properties

191

Equations (5)–(11) define the number density of each compo-
192 nent. However, the signal actually measured with an infrared de-
193 tector is defined by an intensity, I_ν , typically measured in units
194 of MJy sr⁻¹ or nW m⁻² Hz⁻¹ sr⁻¹. The connection between the
195 number density and this thermal emission is modeled in terms of
196 a blackbody modified by an emissivity factor $E_{c,\lambda}$,²
197

$$I_{c,\lambda}^{\text{Thermal}} = E_{c,\lambda} B_\lambda(T), \quad (12)$$

where B_λ is the Planck function at a wavelength λ (Kelsall et al.
198 1998). A key parameter in this equation is the IPD temperature
199 T , which is assumed to fall off with radial distance r (in AU)
200 from the Sun as
201

$$T(r) = T_0 r^{-\delta}, \quad (13)$$

where T_0 is the temperature of IPD at 1 AU and δ is a power-law
202 exponent which is expected to be ~ 0.5 for gray dust. In addition
203 to emitting thermally, IPD grains also scatter sunlight in near-
204 infrared wavelengths. The contribution to the total signal from
205 scattering reads
206

$$I_{c,\lambda}^{\text{Scattering}} = A_{c,\lambda} F_\lambda^\odot(r) \Phi(\Theta), \quad (14)$$

where $A_{c,\lambda}$ is the albedo (or reflectivity) of the IPD, $F_\lambda^\odot(r)$ the
207 solar flux at a radial distance from the Sun, and $\Phi(\Theta)$ is the so-
208 called phase function for scattering angles Θ , which describes
209 the angular distribution of the scattered light. **In particular, our**
210 **ZL model features a Henyey-Greenstein phase function as**
211 **defined by Hong (1985):**
212

$$\Phi(\Theta) = \sum_{k=1}^3 w_k \frac{1}{4\pi} \frac{1 - g_k^2}{(1 + g_k^2 - 2g_k \cos(\Theta))^{3/2}}, \quad (15)$$

where g_1 , g_2 , g_3 , w_2 , and w_3 are free parameters, while
213 $w_1 = 1 - (w_2 + w_3)$.

² In these expressions, λ denotes wavelength channel, and may be re-
ferred interchangeably to both the physical wavelength and the DIRBE
channel ID, e.g., channel 1 corresponds to 1.25 μm ; see Hauser et al.
(1998) for a full definition.

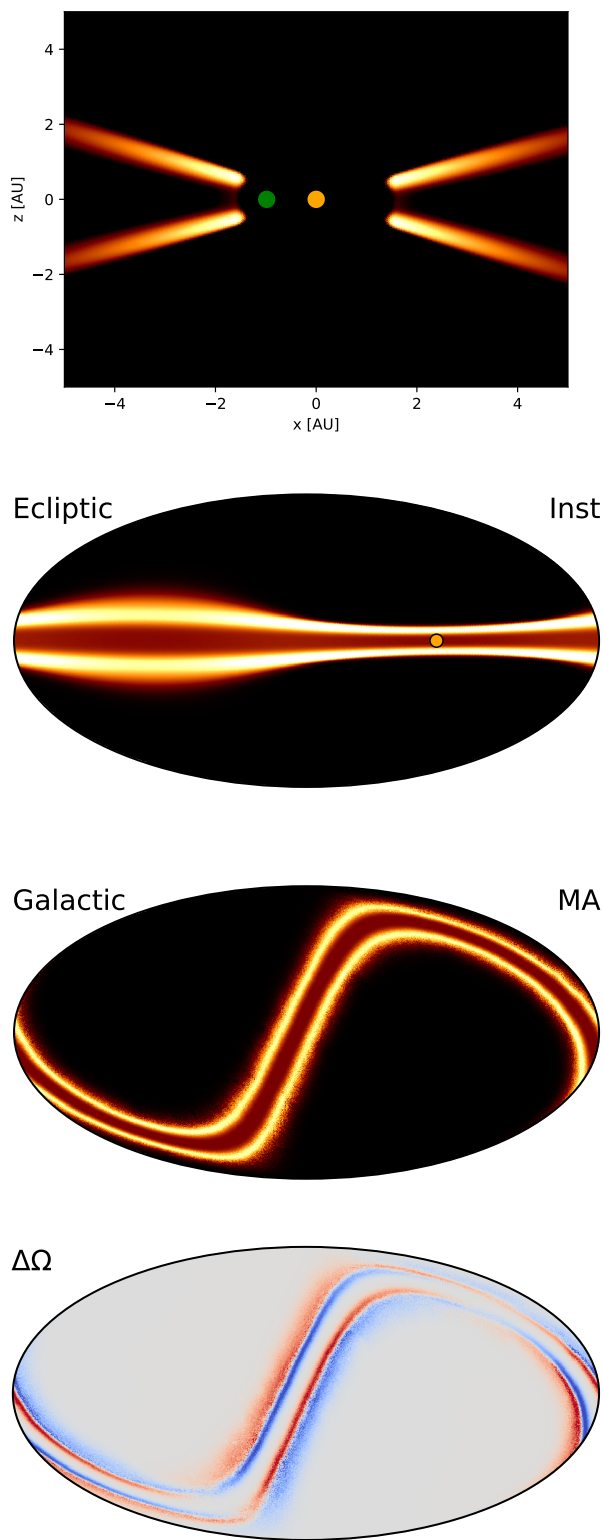


Fig. 1. Geometry of the **first** asteroidal dust band. (*First row:*) Slice through the x - z plane of the number density, n_0 , in heliocentric coordinates. The positions of the Sun and Earth are marked by orange and green dots, respectively. (*Second panel:*) Observed instantaneous intensity plotted in Ecliptic coordinates, obtained by integrating the above figure along each line-of-sight. (*Third row:*) Same as above, but plotted in Galactic coordinates and mission averaged (MA) over nearly a full year of observations corresponding to the DIRBE scanning strategy. (*Fourth row:*) **Difference** between observed intensities as defined in the third row after changing the value of the ascending node, Ω , by 5 %. Similar plots for all components and parameters are provided in Appendices A and B.

Article number, page 4 of 27

The total intensity from a single IPD grain is then

$$I_{c,\lambda}^{\text{Total}} = I_{c,\lambda}^{\text{Scattering}} + I_{c,\lambda}^{\text{Thermal}} \quad (16)$$

$$= A_{c,\lambda} F_\lambda^\odot \Phi + (1 - A_{c,\lambda}) E_{c,\lambda} B_\lambda, \quad (17)$$

where we have also taken into account that reflective material have lower thermal emission by introducing a factor $(1 - A_{c,\lambda})$ to the thermal term. The total ZL signal may then be evaluated by summing up the intensity from all dust grains, which in practice means evaluating a line-of-sight integral for each observation,

$$I_{p,t,\lambda} = \sum_c \int n_c [A_{c,\lambda} F_\lambda^\odot \Phi + (1 - A_{c,\lambda}) E_{c,\lambda} B_\lambda] ds. \quad (18)$$

Here, p represents an observed pixel or direction in the sky, t is the time of observation; n_c is the number density of component c in the line-of-sight; and ds is a small distance along the line-of-sight s from the observer and toward p .

Due to the limited signal-to-noise ratios, we follow Kelsall et al. (1998) and only fit one overall albedo for each high-frequency channel, as well as only one common emissivity for all three asteroidal bands.

2.4. Model intuition

As described above, **our model** has only $O(10^2)$ free parameters, which we collectively denote ζ_z . Clearly, this is in reality far too few to fully capture the true complex nature of ZL across many decades in wavelength. However, even with such a limited number of parameters, the model is still severely under-constrained when fitted to the DIRBE data, and the corresponding posterior distribution exhibits many strong degeneracies. Consequently, most currently available parameter estimation algorithms are prone to getting trapped in local posterior maxima, and this then will result in significant residuals in the final ZL cleaned maps.

In order to interpret such residuals, and potentially define better starting points for the non-linear optimization algorithm, it is useful to build up human visual intuition regarding the impact of each free parameter. Figure 1 shows one specific (and arbitrary) example of this. First, the top panel shows a x - z -plane slice through the three-dimensional IPD number density distribution for the **first dust band**, B_1 . In this figure, the orange dot marks the Sun's position, while the green dot marks the observer's (or Earth's) position. Here it is worth noting that this component is azimuthally symmetric about the Sun, and the full 3D structure may therefore be visualized by rotating this figure about the vertical z -axis. In this space, it is quite straightforward to visualize the effect of each free parameter defined by Eq. (9). For instance, the position of the inner radial cut-off can be changed by modifying δ_r , while the angle between the x -axis and the peak densities may be changed through δ_ζ . If we modify the x_0 offset, the entire density field will shift left or right.

The second panel in Fig. 1 shows the corresponding signal in Ecliptic coordinates at one single point in time after integrating the density field along each line-of-sight. The Sun's position is again marked by an orange dot, but in this case there is obviously no observer position, since this figure shows the sky as seen outward from the observer. In this projected 2D space, the observed structures appear significantly more difficult to visualize than in 3D space. For instance, while the density of the dust bands appear symmetric in 3D space, their apparent separation and width as seen from Earth vary significantly with Ecliptic longitude, as seen in the second panel; they appear narrower when looking toward the Sun, where the bands are physically further away from the Earth, and broader closeby.

270 The third panel shows the same feature, but now averaged
 271 over nearly a whole year of observations, corresponding to the
 272 DIRBE scanning strategy, and plotted in Galactic coordinates.
 273 This represents the signal seen in full-mission maps derived from
 274 DIRBE. Since the underlying IPD structure is azimuthally sym-
 275 metric about the Sun, the Earth's movement throughout the year
 276 also symmetrizes the total co-added signal, and the dust bands
 277 once again appear symmetric about the Ecliptic plane. However,
 278 some small-scale structures also appear because of small varia-
 279 tions in the effective scanning path of the instrument from day
 280 to day; if an entire day's worth of observations were missing, for
 281 instance due to a period of excessive cosmic ray radiation, strong
 282 stripes would appear in this map.

283 With the infrastructure for computing such full-mission
 284 maps ready at hand, we can study the impact of each free param-
 285 eter in greater detail. As a specific example of this, the bottom
 286 panel in Fig. 1 shows the **difference** between the total signal ob-
 287 tained when changing the ascending node Ω for **Band 1** by 5 %
 288 relative to a **suitable set of parameters for our ZL model**. In-
 289 tuitively, this corresponds to rotating the signal in the top figure
 290 slightly about the origin. Some parts of the bands will then ap-
 291 pear closer to the Earth, while others will appear further away.
 292 Those regions then in turn appear either red or blue in the bot-
 293 tom figure. The resulting pattern is a unique signature for Ω , and
 294 if similar structures are observed in the final ZL cleaned maps,
 295 then one should consider modifying this particular parameter in
 296 a future analysis.

297 Similar figures are provided for all components and all pa-
 298 rameters in Appendices A and B, and these are very useful for
 299 building up visual intuition regarding the **ZL model in use**.
 300 Quickly scanning through the individual panels in Figs. B.1 and
 301 B.2, we can already now identify strong degeneracies that are
 302 likely to turn out to be problematic later. For instance, we see
 303 that $n_{0,C}$, α_C , $n_{0,SR}$, T_0 , and δ are all dominated by a ring cen-
 304 tered along the Ecliptic plane, and these are likely to interplay
 305 significantly. Furthermore, many of these parameters, such as
 306 $n_{0,C}$, $\sigma_{z,SR}$, and $\sigma_{\theta,TF}$, will obviously also couple significantly to
 307 a wide range of non-ZL type parameters when integrated into
 308 a global analysis framework, including the all-important CIB
 309 monopoles.

310 2.5. Numerical optimizations

311 Performing the line-of-sight integrals defined by Eq. (18) is an
 312 expensive part in the COSMOGLOBE DR2 analysis pipeline already
 313 for the DIRBE data, which only comprise 18 GB after compres-
 314 sion. In principle, this could be done by brute-force for this par-
 315 ticular experiment on modern computer clusters, but such a di-
 316 rect approach will clearly not be an option for similar analyses
 317 of *Planck* HFI, *AKARI*, and *SPHEREx*.

318 When sampling parameters for the ZL model it is possible
 319 to include only a small fraction of the full dataset in each likeli-
 320 hood evaluation, simply because the signal-to-noise ratio of each
 321 sample is so high, and because of the smooth ZL gradient of the
 322 ZL structure. Intuitively speaking, white instrumental noise is
 323 irrelevant compared to overall systematic model uncertainties,
 324 and some number of consecutive time-domain samples therefore
 325 provide essentially the precisely same information. In our cur-
 326 rent analysis, we adopt a thinning factor of eight, meaning that
 327 we effectively fit the data to a time-stream sampled at 1 Hz rather
 328 than the original 8 Hz DIRBE CIO. In principle, we could have
 329 averaged over this time segment, rather than simply omitting the
 330 relevant samples, in order to suppress instrumental noise; and, in
 331 fact, the first implementation of our computer code did exactly

332 this. However, averaging over 1 sec time scales implies that the
 333 true underlying model is also smoothed out the same time scales,
 334 and this increases the overall modeling errors. Although the dif-
 335 ferences were generally small, we obtained slightly better fits by
 336 thinning rather than averaging.

337 A second optimization step is introduced by dividing the pa-
 338 rameters in ζ_z into a set of so-called sampling groups, and esti-
 339 mating the free parameters in each group separately. Specifically,
 340 it is worth noting that the overall signal-to-noise ratio for the ZL
 341 component shape parameters, such as Ω_C or δ , is vastly domi-
 342 nated by the **12, 25, and 60 μ m channels**. At the same time, the
 343 emissivity and albedo for a given channel depend only on that
 344 same channel, and it is therefore not necessary to process, say,
 345 the $1.25 \mu\text{m}$ TOD when estimating the $4.9 \mu\text{m}$ albedo. In prac-
 346 tice, we therefore first estimate all ZL shape parameters (and the
 347 corresponding emissivities, albedos and monopoles) using only
 348 the **12, 25, and 60 μ m channels**, and then we estimate the emis-
 349 sivity, albedo, and monopole for each of the remaining chan-
 350 nels separately — but now conditionally on the shape param-
 351 eters derived **before**. The cost of this approach is slightly higher
 352 statistical uncertainties on the shape parameters, since the other
 353 channels could have contributed with some information for these
 354 parameters as well, but the gain is a computational speed-up of
 355 roughly one order-of-magnitude, and we consider this an excel-
 356 lent trade-off.

3. Methods

357 The main operational goal of this paper is to measure the free ZL
 358 parameters, ζ_z , using time-ordered data from the DIRBE instru-
 359 ment. However, these data contain many other physical effects in
 360 the form of both instrumental and astrophysical confusion (e.g.,
 361 Hauser et al. 1998; Arendt et al. 1998). In order to estimate ζ_z
 362 robustly, it is essential to account for all those other degrees of
 363 freedom at the same time. On the other hand, many of those pa-
 364 rameters have only a limited signal-to-noise ratio with DIRBE
 365 data alone, and far stronger constraints will typically result from
 366 combining the DIRBE measurements with external data. En-
 367 abling such global multi-experiment analysis is a main goal of
 368 the COSMOGLOBE framework (Gerakakis et al. 2023). In this sec-
 369 tion, we briefly review the key ideas behind this approach, and
 370 we describe the generalizations that are required for ZL param-
 371 eter estimation. For full details, we refer the interested reader to
 372 Watts et al. (2023, 2024a). However, we emphasize that the ap-
 373 proach presented here is only a first step, and future work should
 374 aim at implementing faster and more robust algorithms.

3.1. Data model, posterior distribution, and Gibbs sampling

376 The first step in many Bayesian parameter estimation methods
 377 is to write down an explicit parametric data model. For Cos-
 378 MOGLOBE DR2, we adopt the following model,

$$\mathbf{d} = \mathbf{GB} \left[\mathbf{P} \sum_{c=1}^{n_{\text{comp}}} \mathbf{M}_c \mathbf{a}_c + \mathbf{s}_{\text{zodi}} + \mathbf{s}_{\text{static}} \right] + \mathbf{n} \quad (19)$$

$$\equiv \mathbf{s}^{\text{tot}} + \mathbf{n}, \quad (20)$$

380 where \mathbf{d} denote observed data; \mathbf{G} denotes an overall calibration
 381 factor; \mathbf{P} and \mathbf{B} represent the instrumental pointing and beam,
 382 respectively; the sum over components c represents the contri-
 383 bution from astrophysical components (thermal dust, free-free,
 384 starlight emission etc.), each described by an overall amplitude
 385 (which may be a pixelized map) and a mixing matrix, \mathbf{M} , which

depends on some set of unknown SED parameters, β ; and \mathbf{n} denotes instrumental noise. We further define \mathbf{a}_{sky} and β_{sky} to be the set of all astrophysical component amplitudes and spectral parameters, and ξ_n to be the set of all free instrumental noise parameters. We also define $\mathbf{a}_{\text{static}}$ by $\mathbf{s}_{\text{static}} = \mathbf{P}_{\text{sol}} \mathbf{a}_{\text{static}}$, where \mathbf{P}_{sol} is the pointing in solar-centric coordinates. Finally, we denote the set of all free parameters in Eq. (19) by ω , and for a full explicit definition of this parameter set, we refer the interested reader to [Watts et al. \(2024a\)](#). **Details regarding the foreground model are provided by Galloway et al. (2026); Gjerløw et al. (2026a); Sullivan et al. (2026); Gjerløw et al. (2026b).**

As far as this paper is concerned, the key term is \mathbf{s}_{zodi} , which is nothing but Eq. (18) evaluated along the line-of-sight defined by the pointing \mathbf{P} . This term depends on ζ_z , and our task in this paper is to establish an approximation to the marginal posterior distribution, $P(\zeta_z | \mathbf{d})$. One straightforward way of computing this marginal distribution is, perhaps somewhat surprisingly, to first consider the much bigger task of estimating the full joint posterior distribution, $P(\omega | \mathbf{d})$ — which now includes billions of correlated parameters rather than just a hundred. The reason this is a more straightforward problem, computationally speaking, is that that the joint distribution has a well-defined and simple analytic expression that it is possible to sample from, while the marginal distribution does not; for early CMB applications of this two-stage approach, see [Jewell et al. \(2004\)](#); [Wandelt et al. \(2004\)](#); [Eriksen et al. \(2004\)](#).

In order for this to work, we have to assume that the instrumental noise, $\mathbf{n} = \mathbf{d} - \mathbf{s}_{\text{tot}}$, is Gaussian, and for most instruments that is an excellent approximation. In that case, we can write the likelihood, $\mathcal{L}(\omega) \equiv P(\mathbf{d} | \omega)$, as

$$-2 \ln \mathcal{L}(\omega) = (\mathbf{d} - \mathbf{s}^{\text{tot}}(\omega))' \mathbf{N}_w^{-1} (\mathbf{d} - \mathbf{s}^{\text{tot}}(\omega)) \equiv \chi^2(\omega), \quad (21)$$

and the posterior distribution is then defined by Bayes' theorem,

$$P(\omega | \mathbf{d}) = \frac{P(\mathbf{d} | \omega)P(\omega)}{P(\mathbf{d})} \propto \mathcal{L}(\omega)P(\omega). \quad (22)$$

Here $P(\omega)$ is called the prior, which may be used to inject prior knowledge about given parameters, while $P(\mathbf{d})$ is called the evidence, which for our purposes is just a normalization constant.

In order to map out this full joint posterior, we use a statistical method called Gibbs sampling (e.g., [Geman & Geman 1984](#)), which allows us to draw samples iteratively by scanning through all conditional distributions, as opposed to drawing samples directly from the joint distribution. Sampling from N conditional distributions, each defined by a simple analytical distribution, is typically much simpler than drawing from a single joint N -dimensional distribution that does not have a closed form analytical expression. In practice, for the COSMOGLobe DR2 analysis this translates into the following so-called Gibbs chain:

$$\mathbf{G} \leftarrow P(\mathbf{G} | \mathbf{d}, \xi_n, \beta_{\text{sky}}, \mathbf{a}_{\text{sky}}, \zeta_z, \mathbf{a}_{\text{static}}) \quad (23)$$

$$\xi_n \leftarrow P(\xi_n | \mathbf{d}, \mathbf{G}, \beta_{\text{sky}}, \mathbf{a}_{\text{sky}}, \zeta_z, \mathbf{a}_{\text{static}}) \quad (24)$$

$$\beta_{\text{sky}} \leftarrow P(\beta_{\text{sky}} | \mathbf{d}, \mathbf{G}, \xi_n, \mathbf{a}_{\text{sky}}, \zeta_z, \mathbf{a}_{\text{static}}) \quad (25)$$

$$\mathbf{a}_{\text{sky}} \leftarrow P(\mathbf{a}_{\text{sky}} | \mathbf{d}, \mathbf{G}, \xi_n, \beta_{\text{sky}}, \zeta_z, \mathbf{a}_{\text{static}}) \quad (26)$$

$$\zeta_z \leftarrow P(\zeta_z | \mathbf{d}, \mathbf{G}, \xi_n, \beta_{\text{sky}}, \mathbf{a}_{\text{sky}}, \mathbf{a}_{\text{static}}) \quad (27)$$

$$\mathbf{a}_{\text{static}} \leftarrow P(\mathbf{a}_{\text{static}} | \mathbf{d}, \mathbf{G}, \xi_n, \beta_{\text{sky}}, \mathbf{a}_{\text{sky}}, \zeta_z), \quad (28)$$

where \leftarrow indicates the process of drawing a sample from the distribution on the right-hand side. Each sampling step in this chain is described by [Watts et al. \(2024a\)](#) and references therein — except for Eq. (27), which is the main topic of this paper.

Based on the data model in Eq. (19), we can define the following residual

$$\mathbf{r} = \mathbf{d} - (\text{GPB} \sum_{c=1}^{n_{\text{comp}}} \mathbf{M}_c \mathbf{a}_c + \mathbf{s}_{\text{static}}), \quad (29)$$

and this should ideally only contain ZL and noise. As such, the assumed Gaussianity of the noise also defines the conditional distribution in Eq. (27), and we may write

$$-2 \ln P(\zeta_z | \mathbf{d}, \dots) = \sum_v \left(\frac{\mathbf{r}_v - \mathbf{s}_{v, \text{zodi}}(\zeta_z)}{\sigma_v} \right)^2 \equiv \chi^2(\zeta_z), \quad (30)$$

where we have introduced multiple data frequency channels, denoted by v , and also for simplicity neglected the prior, $P(\zeta_z)$. We also define the reduced chi-squared $\chi_{\text{req}}^2 = \chi^2 / n_{\text{TOD}}$, where n_{TOD} is the number of TOD samples included in the likelihood evaluation. In this framework, ZL parameter estimation is thus nothing but a traditional Gaussian χ^2 optimization (or sampling) problem after all non-ZL contributions have been subtracted from \mathbf{d} . Precisely how we implement this operation in the current pipeline is described in Sect. 3.3.

So far we have silently skipped past one important term in Eq. (19), namely $\mathbf{s}_{\text{static}}$, which is discussed in detail by ([Watts et al. 2024a](#)). As noted by [Hauser et al. \(1998\)](#) and [Kelsall et al. \(1998\)](#), the DIRBE TOD contain significant excess radiation that is not well described by the low-dimensional parametric K98 model. Shortly after these observations, [Leinert et al. \(1998b\)](#) showed that some of this radiation appeared to be stationary in solar-centric coordinates; see their Figure 54. Such radiation can in principle be created through several different physical mechanisms. For instance, a yet unknown zodiacal component could create a signal that appears stationary in solar-centric coordinates, just like the circular-solar ring described in Sect. 2.2.3, or it could also be caused by stray-light contamination in the DIRBE optics. However, even though this radiation was first noted more than two decades ago, it was never mapped out systematically until now, as part of the current COSMOGLobe DR2 analysis ([Watts et al. 2024a](#)). For the time being, we choose to remain agnostic regarding the physical origin of this signal, and therefore, strictly speaking, the ZL model presented in the current paper only describes the parts of the total observed ZL that is attributable to the K98 parametrization. In the future, it is possible that the static component presented by [Watts et al. \(2024a\)](#) should also be added to this model. However, before that is done, it is imperative to rule out the stray-light hypothesis, and that will require both detailed modeling of the DIRBE instrument and joint analysis with other experiments, such as *AKARI*, *IRAS*, *Planck* HFI, and SPHEREx. Doing that is beyond the scope of the current COSMOGLobe data release, but it will certainly be a main topic for future work.

Related to this, we also note that the circumsolar ring and trailing feature discussed in Sect. 2.2.3 are completely degenerate with a general pixelized static component in solar-centric coordinates, and it is therefore not possible to fit these and the excess radiation component simultaneously. For this reason, we fix the circumsolar ring and trailing feature parameters at their K98 values, and note that these will have to be revisited once a physical model for the excess radiation has been established.

3.2. Comparison with K98 fitting algorithm

Before describing the practical numerical implementation used for sampling from Eq. (27) in this paper, it is worth first considering the more important fundamental differences between our

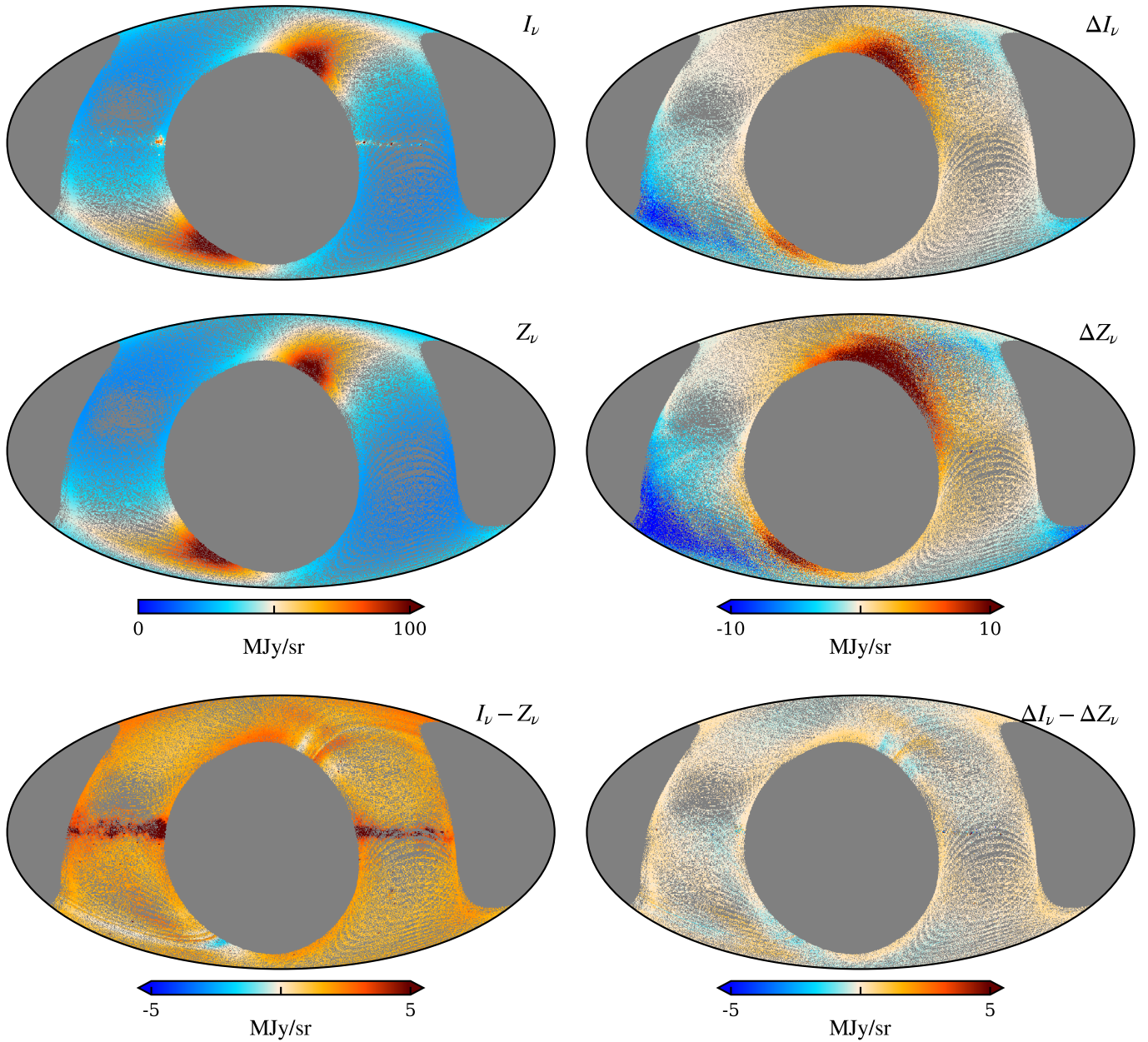


Fig. 2. Illustration of the basic sky maps involved in the ZL fitting algorithms adopted by the COSMOGLOBE (left column) and K98 (right column) pipelines for one week of $25\mu\text{m}$ observations, both adopting the K98 model. The basic data element in COSMOGLOBE is the full sky signal, I_ν (top left), which is fitted with the full ZL model (K98 in this case), Z_ν (middle left), both modeled in time-domain. The χ^2 used in the COSMOGLOBE analysis minimizes the total signal-minus-model residual, $I_\nu - Z_\nu$ (bottom left). In contrast, the K98 pipeline used exclusively differences between weekly and full-season maps, both for the observed signal, $\Delta I_\nu \equiv I_\nu - \langle I_\nu \rangle$ (top right), and the ZL model, $\Delta Z_\nu = Z_\nu - \langle Z_\nu \rangle$ (middle right), where brackets indicate full-survey averages. Correspondingly, the final χ^2 is defined through $\Delta I_\nu - \Delta Z_\nu$ (bottom right), and is by construction only sensitive to time-variable signals. The main advantage of the K98 approach is insensitivity to stationary sky signals, in particular thermal dust and CIB, while the main advantage of the COSMOGLOBE approach is a much higher effective signal-to-noise ratio, both to ZL parameters and zero-levels, as seen by comparing the two bottom panels.

approach and that adopted by the DIRBE team as described by Kelsall et al. (1998). The first difference worth noting in this respect is that while our χ^2 statistic is defined directly in terms of TOD, the K98 parameter estimation method works with weekly maps. That is, the raw data are co-added week-by-week into pixelized maps, and these are fed into a corresponding pixel-based χ^2 statistic. One important motivation for working with weekly maps rather than single TOD samples is lower computational re-

quirements, which was more important two decades ago than it is today.

A second important difference between the two algorithms – and this is conceptually a far more important one – is the fact that while our method makes active use of an explicit parametric data model for all non-ZL components, the K98 algorithm eliminates any contributions from non-ZL components by only considering differences between weekly maps and the corresponding full-mission average map in their χ^2 statistic. That is, rather

507 than optimizing the full χ^2 as defined in Eq. (30), their algorithm
 508 optimizes

$$-2 \ln P_{\text{K98}}(\zeta_z | \mathbf{d}, \dots) = \sum_{i,v} \left(\frac{\Delta \mathbf{d}_{i,v} - \Delta \mathbf{s}_{i,v,\text{zodi}}(\zeta_s)}{\sigma_v} \right)^2 \quad (31)$$

$$\equiv \chi^2_{\text{K98}}(\zeta_z), \quad (32)$$

509 where i indicate week number, $\Delta \mathbf{d}_{i,v} = \mathbf{d}_{i,v} - \langle \mathbf{d}_{i,v} \rangle$, $\Delta \mathbf{s}_{i,v,\text{zodi}} =$
 510 $\mathbf{s}_{i,v,\text{zodi}} - \langle \mathbf{s}_{i,v,\text{zodi}} \rangle$, and brackets denote averaging over the full
 511 mission.

512 Clearly, this statistic has a key philosophical advantage as
 513 compared to the full-signal statistic in Eq. (30): it does not re-
 514 quire any assumptions regarding the astrophysical nature of a
 515 complicated infrared sky. At least to first order, it is by construc-
 516 tion safe against biases from foreground modeling errors. How-
 517 ever, this bias immunity also comes at a massive cost in terms of
 518 statistical uncertainties, because it is not only immune to astro-
 519 physical bias, but it is also by construction blind to the monopole
 520 created when producing mission averaged maps, which can be as
 521 bright as 20 MJy/sr at the 25 μm channel ZL signal, meaning that
 522 a lot of signal-to-noise is lost with this approach.

523 Figure 2 illustrates this difference. The top left panel shows
 524 the full intensity signal as analyzed in the COSMOGLOBE algorithm
 525 for one single week of 25 μm observations. The visual imprint is
 526 strongly dominated by the ZL features as seen in the total instant-
 527 aneous ZL view in Appendix A, aligned with the Ecliptic plane.
 528 The right panel shows the same after subtracting the full-mission
 529 mean; the characteristic cloud pattern has now turned into differ-
 530 ential structures that are difficult to interpret visually. The middle
 531 row shows the same for the **ZL signal as predicted by the K98**
 532 **model**, and the bottom row shows the difference between the top
 533 and middle rows, which serves as the input to the χ^2 evaluations.

534 Several points are worth noting in these figures. First of all,
 535 we immediately note that the color scale is one order of magni-
 536 tude narrower in the right column than in the left column; this
 537 will translate directly into lower constraining power for the dif-
 538 ferential approach.

539 Second, we see that the Galactic plane signal represents a
 540 strongly sub-dominant component in the total signal amplitude.
 541 Even relatively large errors made in the model assumptions of
 542 these will have a very small impact on the overall ZL estimates,
 543 and it is also straightforward to mitigate this effect further by
 544 masking out any samples that are close known bright Galactic
 545 sources; this is fully equivalent to what is done in the CMB field
 546 when estimating the CMB power spectrum.

547 Third, as seen in the bottom panel, the $\chi^2_{\text{K98}}(\zeta_z)$ is also by
 548 construction entirely blind to the zero-level of the ZL model: the
 549 large relative monopole error between the data and the model
 550 seen in the bottom right panel is entirely suppressed in the bot-
 551 tom left panel, and there is by construction no way for the dif-
 552 ferential method to constrain the absolute level ZL monopole.
 553 On the one hand, such blindness may certainly be considered
 554 to be an algorithmic strength, as indeed argued by Kelsall et al.
 555 (1998), given that one of the main goals of the entire DIRBE ex-
 556 periment was to precisely measure the CIB monopole spectrum
 557 (Hauser et al. 1998). Nevertheless, the final derived CIB con-
 558 straints do of course still depend directly on reconstructed ZL
 559 monopole, whatever it may be. Intuitively speaking, the differ-
 560 ential method aims to measure the ZL monopole using derivatives
 561 alone. Whether that task is easier or harder than to establish a
 562 sufficiently accurate model of the Milky Way can only be de-
 563 termined by trying both methods, and comparing the results. In
 564 addition, it is also worth noting that derivative measurements in

565 general are far more susceptible to systematic biases from any
 566 non-Galactic source than absolute intensity measurements. One
 567 important example in this respect is optical non-idealities. 568

3.3. Posterior sampling by non-linear optimization

To complete the algorithm in Sect. 3.1, we still need to specify
 569 the details of the algorithm used to draw samples from Eq. (27).
 570 A broad range of Bayesian sampling methods can be envisioned
 571 used for this purpose, from simple Metropolis-Hastings (MH)
 572 accept-reject samplers to various incarnations of Hamiltonian
 573 samplers that exploit derivative information. Indeed, our very
 574 first implementation employed a simple MH sampler with man-
 575 ually tuned step lengths, and this was used for early model ex-
 576 ploration and code testing. However, this approach was quickly
 577 abandoned because it, after a short burn-in period, very quickly
 578 got stuck in a local minimum, and all subsequent proposed sam-
 579 ples were rejected. 580

As noted already in Sect. 2, the main challenge with the ZL
 581 posterior distribution is a large number of degeneracies. These
 582 translate into a highly structured posterior distribution with many
 583 local maxima, and it is generally difficult for most iterative non-
 584 linear optimization or MCMC methods to map out such param-
 585 eter spaces efficiently. 586

The original K98 analysis used a standard Levenberg-
 587 Marquardt algorithm to compute the best-fit model. This is a
 588 non-linear optimization algorithm that essentially interpolates
 589 between a Gauss-Newton and a gradient descent algorithm. As
 590 such, that analysis was also susceptible to getting trapped in a
 591 local minimum. 592

In the current paper, we adopt a pragmatic approach to this
 593 problem that uses ideas from both the MH and non-linear opti-
 594 mization approaches. The non-linear optimization step is for
 595 now performed with a simple Powell search, which uses a series
 596 of bi-directional line searches along a set of conjugate directions.
 597 The only reason for choosing this method over, say, Levenberg-
 598 Marquardt was one of implementational ease; it does not require
 599 derivative information. 600

The algorithm is defined as follows: **we start by initializing all free ZL parameters at the values listed in Kelsall et al. (1998) and Hong (1985)**, and run one Powell optimization
 601 to reach the nearest local posterior maximum. We then iterate
 602 through all non-ZL Gibbs steps, to obtain a new foreground and
 603 instrument model given the new ZL model. When returning to
 604 the ZL sampler, we add a Gaussian random fluctuation to each
 605 ζ_z parameter, which for now is defined by an rms of 1 % of its
 606 original value. We then run a new Powell optimization to identify
 607 a new local ZL parameter maximum. This new model is then ac-
 608 cepted or rejected based on the following Metropolis-like accept
 609 probability, 610

$$a = \min \left(e^{-\frac{1}{2} \frac{\chi^2_{\text{red,new}} - \chi^2_{\text{red,old}}}{\delta_a}}, 1 \right), \quad (33)$$

where δ_a is a tunable parameter that determines the strictness of
 613 the rejection criterion. Explicitly, if a proposed ζ_z has a lower
 614 reduced chi-squared χ^2_{red} than the previous sample, it is always
 615 accepted; if it has a higher χ^2_{red} , it is accepted with probability a .
 616 We comment below on the reason this definition uses χ^2_{red} rather
 617 than the absolute χ^2 , as well as how we set a . 618

In practice, many adjustments have been made gradually
 619 over the course of many months and hundreds of short individual
 620 test runs to the COSMOGLOBE DR2 data selection, analysis masks,
 621 and parametric data model. In each case, the new job has been
 622

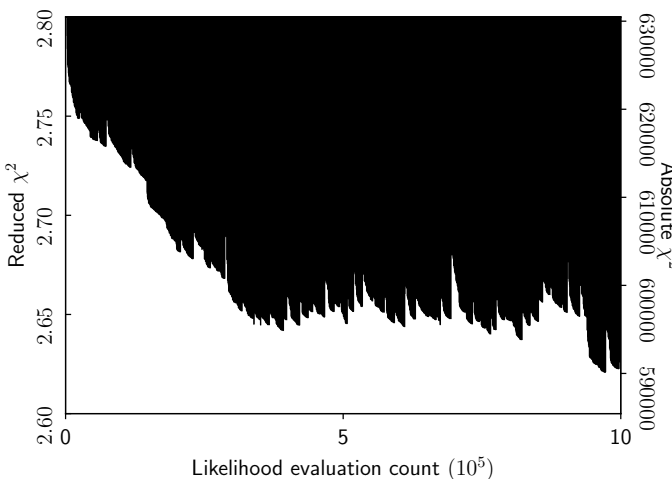


Fig. 3. Reduced χ^2 as a function of Powell likelihood evaluation count for one single pre-production Gibbs chain, showing the burn-in phase. Each discrete jump indicates the start of a new Gibbs sample, which is initialized on a new random point that is close to the previous iteration. The following systematic decline within each main Gibbs iteration indicates the non-linear optimization performed by the Powell algorithm. The solid dark region corresponds to a large number of highly sub-optimal parameter trials.

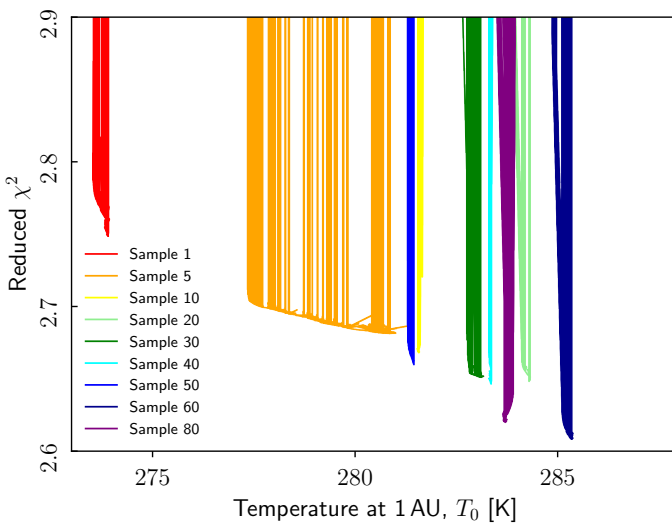


Fig. 4. Reduced χ^2 as a function of the temperature at 1 AU, T_0 for the same run shown in Fig. 3. Each curve shows the full set of parameter trials within one single main Gibbs iteration (or Powell call), and different colors indicate different Gibbs iteration. Redder colors are earlier in the chain.

lustrate the burn-in phase. Each discrete jump corresponds to one new main Gibbs iteration, while the smooth descent between two jumps correspond to the Powell search. The dense black “roof” corresponds to a large number of very poor parameter estimates made within each Powell search. Only the very last point in each block is propagated forward to the rest of the Gibbs chain. Each likelihood evaluation takes about 0.3 sec wall-time on 128 cores, and the evaluations shown in this figure therefore correspond to about 10 000 CPU-hrs.

We see that the burn-in period appears to be roughly 20 main Gibbs iterations, or about 300 000 likelihood evaluations, after which the chain appears reasonably stationary as measured in terms of χ^2 . As for any MCMC sampler, the chain scatters up and down in χ^2 as it explores the overall parameter space, and sometimes worse models than the previous best-fit are accepted.

Further intuition regarding this pseudo-MH algorithm and the underlying multi-peaked likelihood surface is provided in Fig. 4, which again shows χ^2_{red} for a large number of likelihood evaluations. However, this time this is plotted as a function of the overall reference temperature of the IPD cloud, T_0 , and also plotted separately for nine individual main Gibbs samples; the sample numbers are color coded according to a rainbow scheme, such that redder colors are closer to the beginning of the Markov chain. Intuitively, the lower edge of each curve represents a snapshot of the local neighborhood around each likelihood minimum. We note that each such likelihood neighborhood is quite sharp, indicating that the optimization algorithm is traversing a rather narrow “likelihood valley”. At the same time, different samples reach a different absolute minimum level that is not a smooth function of T_0 ; this is because of all the other parameters in ζ_z that are effectively marginalized over in this figure. As far as burn-in and convergence is concerned, we see that the Markov chain moves systematically from its initial value at $T_0 \sim 273$ K to ~ 284 K during the first 20 samples, and after that it moves randomly between 282 and 286 K. In sum, this figure illustrates well the highly complex and multi-peaked likelihood surface that must be explored when sampling ZL parameters.

As noted above, we define the accept/reject criterion in terms of a reduced $\chi^2_{\text{red}} \equiv \chi^2/n_{\text{TOD}}$, rather than the absolute χ^2 , as dictated by the traditional Metropolis-Hastings rule. The reason for this is illustrated in Fig. 3, as both the absolute and reduced χ^2 are shown in the right and left y-axes. The point is simply that the main uncertainties in these evaluations is not white instrumental noise, but rather model errors and residual systematics. As far as overall goodness-of-fit is concerned, all models that are derived in the post-burn-in phase appears visually equally good, despite the fact that the absolute χ^2 varies with $O(10^5)$ from model to model. This quantity is therefore a very poor measure for overall acceptability. In contrast, the reduced χ^2 varies with $O(10^{-3})$ from sample to sample, and that is a much more meaningful measure for overall goodness-of-fit. For now, we conservatively set $\delta_a = 0.1$, and the accept probability in Eq. (33) is then primarily a safe-guard against accepting pathologically poor models that lie outside the range seen in Fig. 3.

It is important to stress that this algorithm — because of the random jump proposal rule, the subsequent non-linear optimization phase, and the accept rule based on a reduced χ^2 — does not formally satisfy the mathematical demands to a Monte Carlo Markov Chain sampler in terms of ergodicity or reversibility. It is therefore not guaranteed to converge to the true posterior distribution, even in the limit of an infinite number of samples. Rather, this algorithm is essentially simply a pragmatic solution that allow the previous strict χ^2 optimization algorithm used by Kelsall et al. (1998) to evade local posterior maxima, and explore larger

restarted on the previous best-fit solution. This process of slow, gradual and continuously supervised improvements also serves as a safe-guard against nonphysical local posterior maxima, and effectively adds a meta-layer of simulated annealing to the overall algorithm. Typically, the test runs were only run for a few full Gibbs iterations, as in one to ten full samples. Then, once the data and model configuration was considered sufficiently mature for production, a longer run with hundreds of samples distributed over multiple chains were produced.

The overall behavior of this hybrid MCMC+optimization algorithm is illustrated in Fig. 3, which shows the χ^2 obtained from the first 10^6 Powell likelihood evaluations in a preliminary analysis run for the $12+25\mu\text{m}$ ZL sampling group; we show the preliminary chain here rather than the final production run to il-

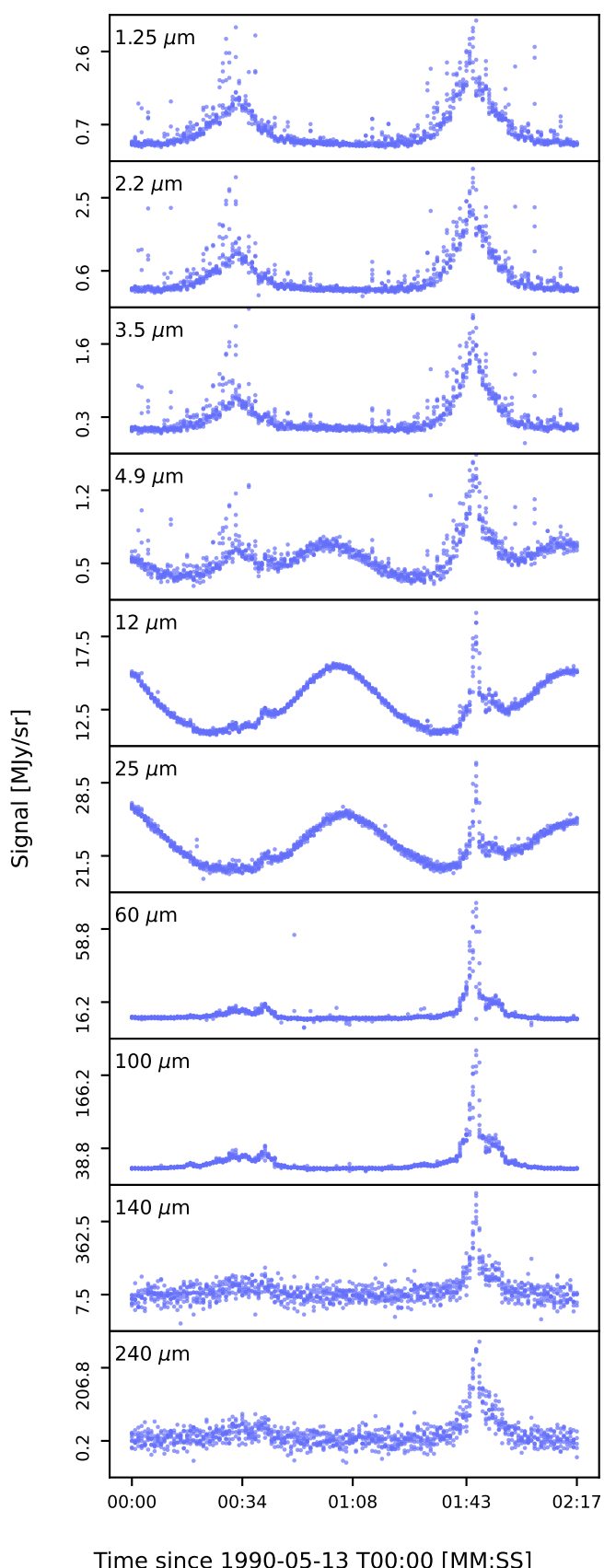


Fig. 5. Subsample of the pre-processed TOD used in this analysis for all ten DIRBE bands. The time-streams show approximately one rotation of the *COBE* satellite which includes two crossing of the Galactic and Ecliptic planes.

regions of parameter space without getting trapped. Significant additional algorithm development efforts should be invested in establishing efficient methods for this particular posterior distribution.

4. Data

4.1. DIRBE Calibrated Individual Observations

The main data set used in the COSMOGLOBE DR2 analysis is the publicly available DIRBE Calibrated Individual Observations (CIO). These are a user-friendly pre-calibrated version of the raw TOD observed by DIRBE. The CIO are pixelized according to the *COBE* Quadrilateral cube projection. As part of the data prepossessing, we convert these to corresponding HEALPix³ (Górski et al. 2005) pixel indices and re-order them into a time-ordered format. We note that the COSMOGLOBE DR2 maps are binned with $7' \times 7'$ pixels, corresponding to a HEALPix resolution of $N_{\text{side}} = 512$, which is substantially higher resolution than the pixel size of $19' \times 19'$ used in the original DIRBE analysis. For full details on the preprocessing of the DIRBE CIO we refer to Watts et al. (2024a).

As already noted by Kelsall et al. (1998), a sharp edge may be seen in the K98 ZSMA $25\mu\text{m}$ map at Galactic coordinates $(l, b) \sim (190^\circ, 15^\circ)$. This corresponds to the very end of the DIRBE observing period. Watts et al. (2024a) studies this effect in greater detail, and we find that this artifact may be mitigated by omitting the last two weeks for the $1.25\text{--}3.5\mu\text{m}$ channels, and the last month for the $4.9\text{--}100\mu\text{m}$ channels. A similar sharp feature may be detected near the start of the survey as well, and we therefore also remove the first week observations in all ten frequency channels. Other features that could be handled in a future release include comet trails, which have been found at the 1% level in the 12 and $25\mu\text{m}$ bands (Arendt 2014).

In addition, to minimize the impact of the excess radiation component, Watts et al. (2024a) define a set of masks in solar-centric coordinates for each frequency channel between 1.25 and $100\mu\text{m}$, and any TOD sample that is excluded by these masks is removed from further analysis. This approach plays exactly the same role as the solar elongation cut used by the DIRBE team to produce their final ZSMA maps, but provides much better precision in terms of removing specific systematic features.

In the following, we will refer to the pre-processed CIO as TOD. A subsample of the TOD for each DIRBE band as used in our analysis can be seen in Fig. 5, where we show data for one rotation of the spacecraft about its boresight. Within this rotation, both the Galactic and Ecliptic planes are crossed twice. The two peaks at around 30 sec and 1 min 45 sec correspond to the Galactic plane crossings, while the sine-like waves in bands 4.9 , 12 , and $25\mu\text{m}$ are due to the ZL emission which peaks in the Ecliptic plane.

In order to trace seasonal ZL modeling errors, we divide the TOD for each DIRBE channel into two, corresponding to the first and second half of the full survey. All ZL parameters are fitted jointly and simultaneously using all data, but the resulting ZL cleaned TOD are binned separately into two independent half-mission maps, and the corresponding half-mission difference maps therefore provide information about seasonal ZL variations not captured by the model.

As summarized by Eq. (19), the COSMOGLOBE DR2 data model includes a wide range of both astrophysical and instrumental parameters. The DIRBE CIO are clearly not

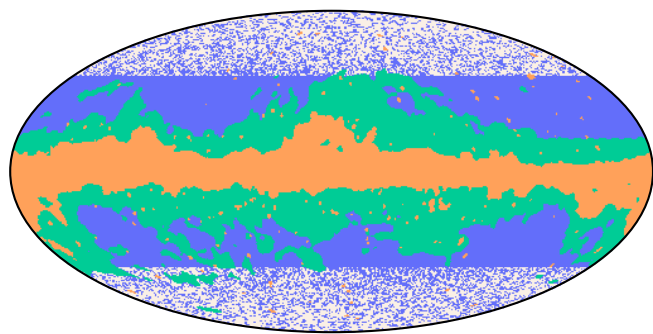


Fig. 6. Three of the processing masks used when estimating ZL parameters. The blue mask is the mask used in the stellar emission dominated $1.25\text{ }\mu\text{m}$ band, the orange mask is used in the ZL dominated $25\text{ }\mu\text{m}$ band, and the green mask is used in the thermal dust dominated $240\text{ }\mu\text{m}$ band.

able to constrain this model very well on their own, and we therefore include ancillary datasets. For full details, see Watts et al. (2024a,b); Galloway et al. (2026); Gjerløw et al. (2026a); Sullivan et al. (2026); Gjerløw et al. (2026b).

4.2. Masks

As discussed in Sect. 3.2, the COSMOGLOBE DR2 parameter estimation algorithm considers the full intensity measured by DIRBE when fitting ζ_z , as opposed to only considering differences between weekly and full-mission maps as Kelsall et al. (1998) did. In order to minimize the risk of confusion from Galactic thermal dust and starlight emission, it is useful to define a confidence mask for each channel that identifies region with a high S/N for ZE, and low S/N for Galactic signals.

For the three channels between 1.25 and $3.5\text{ }\mu\text{m}$, which are strongly dominated by starlight emission, we generate the ZL confidence mask by thresholding the bright compact source model evaluated at $1.25\text{ }\mu\text{m}$ at 20 kJy/sr . In addition we remove all observations with an absolute Galactic latitude $|b| < 45^\circ$. The resulting mask is shown in blue in Fig. 6, and leaves 18 % of the sky available for analysis.

For wavelengths longer than and equal to $60\text{ }\mu\text{m}$, the starlight emission is negligible, and the Galactic signal is instead dominated by thermal dust emission. At these channels, we therefore instead use the sum of the three thermal dust component maps as the main Galactic tracer. For instance, at $100\text{ }\mu\text{m}$ we threshold this map at 3 MJy/sr . In addition, we also remove any pixels for which the absolute data-minus-model residual exceeds a given threshold, which for the $100\text{ }\mu\text{m}$ channel was set to 0.8 MJy/sr . The orange and green pixels in Fig. 6 shows the final masks for the 25 and $240\text{ }\mu\text{m}$ channels, which leaves 81 and 52 % of the sky available for analysis, respectively.

For the intermediate channels between 4.9 and $25\text{ }\mu\text{m}$, we threshold on both diffuse and starlight emission. In all cases, we overlay the final masks on the data-minus-model residual map, and verify by eye that no obvious bright Galactic residuals remain after masking.

5. Results

We are now finally ready to present our new ZL model obtained by analyzing the data summarized in Sect. 4 with the algorithm outlined in Sect. 3. We have produced a total of 1210 full

Gibbs samples, distributed over five Markov chains. A number of samples between 30 and 50, tuned on each parameter individually, was removed from each chain as burn-in, leaving a total of 1060–960 samples for final analysis. In total, 1920 computing cores were used to produce this sample set, for a total cost of about 289k CPU-hrs.

5.1. Markov chains

We start our presentation with a visual inspection of the individual Markov chains for each one of the 36 free ZL parameter in ζ_z . These are shown for the general ZL shape parameters in Fig. 7 and for the amplitude (emissivity and albedo) parameters in Fig. 8. The gray regions indicate the discarded burn-in, which, at this stage, was tuned for each parameter individually.

Note that we are not attempting to fit the geometrical parameters of the three dust bands, but only their number density. In particular, throughout our many attempts, we found that we were unable to constrain the signal in dust band 3 with the DIRBE data alone, as the band would effectively disperse. This phenomenon was previously noted by Spiesman et al. (1995). Moreover, since the degeneracy between T_0 and emissivity created long correlations in previous test runs, here the temperature of IPD at 1 AU was kept fixed at 286 K. The same approach was already adopted by Kelsall et al. (1998).

Examining the trace plots helps to evaluate the degree of convergence for individual parameters. Starting with the shape parameters for the dominant cloud component shown in the leftmost column in Fig. 7, we see that many parameters appear to drift slightly during the first 30–50 samples or so, but after that, they look more stationary. We also see that the mixing between different chains for γ and μ is notably slower than what is common for most Monte Carlo methods discussed in the literature, and this indicates rather long correlation lengths. A similar behavior is observed for the phase function parameters, as shown in the bottom plots in the central column of Fig. 7. Future algorithm development work will aim at decreasing these correlations lengths through better sampling algorithms, as well as reducing the cost per Monte Carlo sample, such that longer Markov chains can be produced. Still, even with the currently available limited sample set, it does appear possible to derive sensible estimates of both the posterior mean and standard deviation for most parameters. It should be noted that the initial value for these parameters are the best-fit parameters of previous trial runs and not the final K98 parameters.

Looking at the dust bands parameters (uppermost plots in the central column of Fig. 7), it is worth noting that the number density of dust band 3 seems to be reaching a prior. As already pointed out, with the DIRBE data this band is very faint and cannot be robustly measured. Therefore, we aim here to constrain an upper limit for it, rather than attempting to provide a point estimate. A similar effect characterizes the g_3 phase function parameter, which consequently appears to be prior-determined.

Regarding the emissivity and albedo parameters shown in Fig. 8, we see much of the same quantitative behavior. A slight drift is always visible during burn-in, which was set to 30 samples for all parameters a part from the emissivity at $240\text{ }\mu\text{m}$ and the albedos that required more time to converge, but then all the traceplots seem quite stable. Long correlation lengths are noticeable in the albedoes plots,

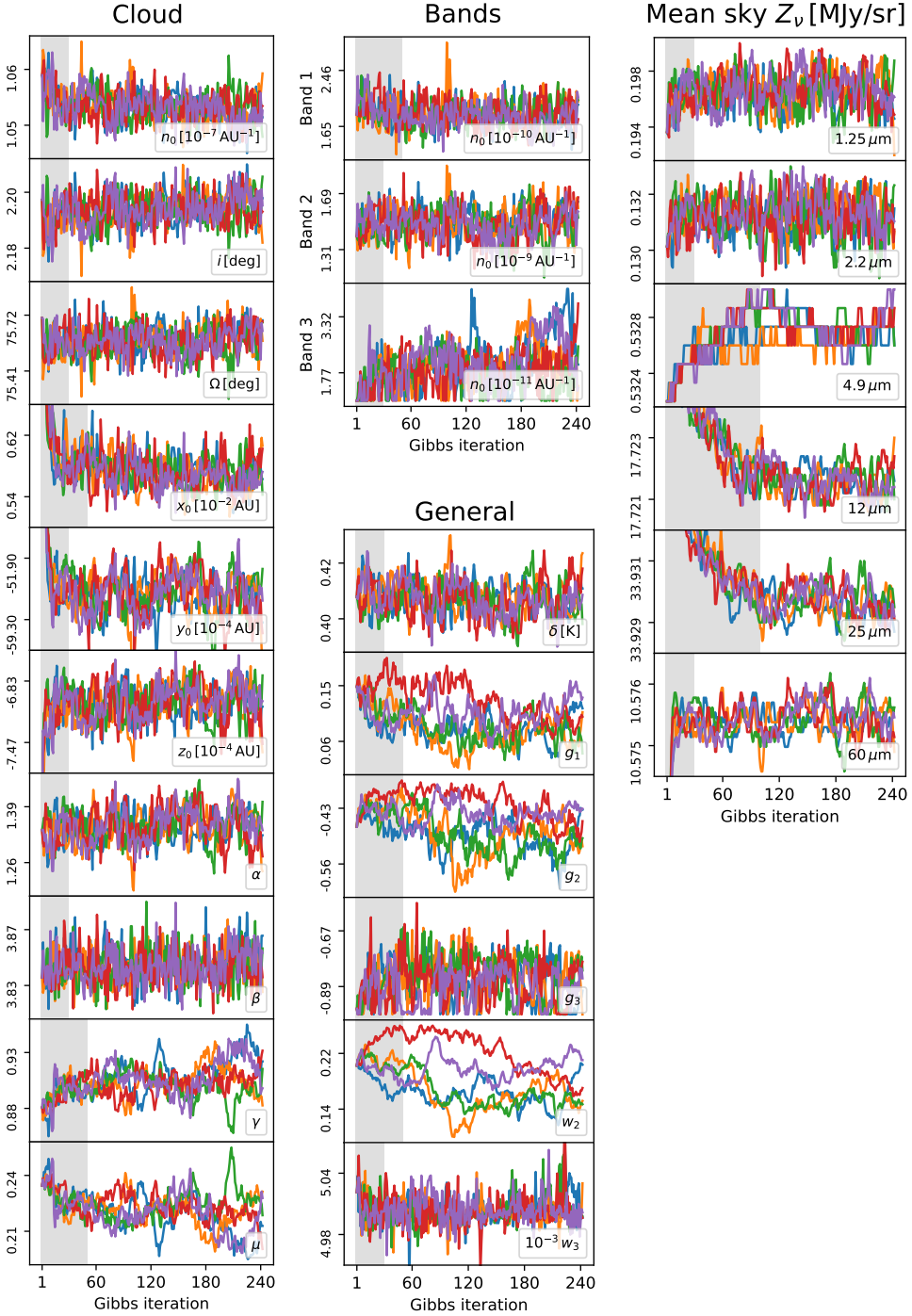


Fig. 7. Trace plots of all geometrical and shape IPD parameters, along with the power-law exponent of the IPD temperature, the phase function parameters, and the full-sky averaged ZL intensity traces for six selected DIRBE channels. Different colors indicate five independent Markov chains, the gray regions indicate the burn-in set for each parameter, and vertical axes were cropped to emphasize convergence.

which could benefit from the algorithmic improvements already noted.

Because of the combination of a very low absolute ZL signal-to-noise ratio of the far-infrared DIRBE channels with strong diffuse Galactic thermal dust emission, there are strong degeneracies between the ζ_z and the Galactic model, which are explored rather inefficiently with the current Gibbs sampler. A future implementation of this framework could consider fitting an overall parametric function for the ZL SED that is smooth in

wavelength, rather than free amplitudes at each channel such that the low S/N channels are supported by the stronger ZL channels in the mid-infrared regime. In addition, we note that only the sum over all ZL components matters for cosmological analysis, not each individual component, and internal degeneracies are therefore of lower overall concern.

Figure 9 shows the Pearson correlation coefficient between pairs of parameters in ζ_z , evaluated directly from the post-burn-in Gibbs sample set. Here, the burn-in was set to 50 samples to

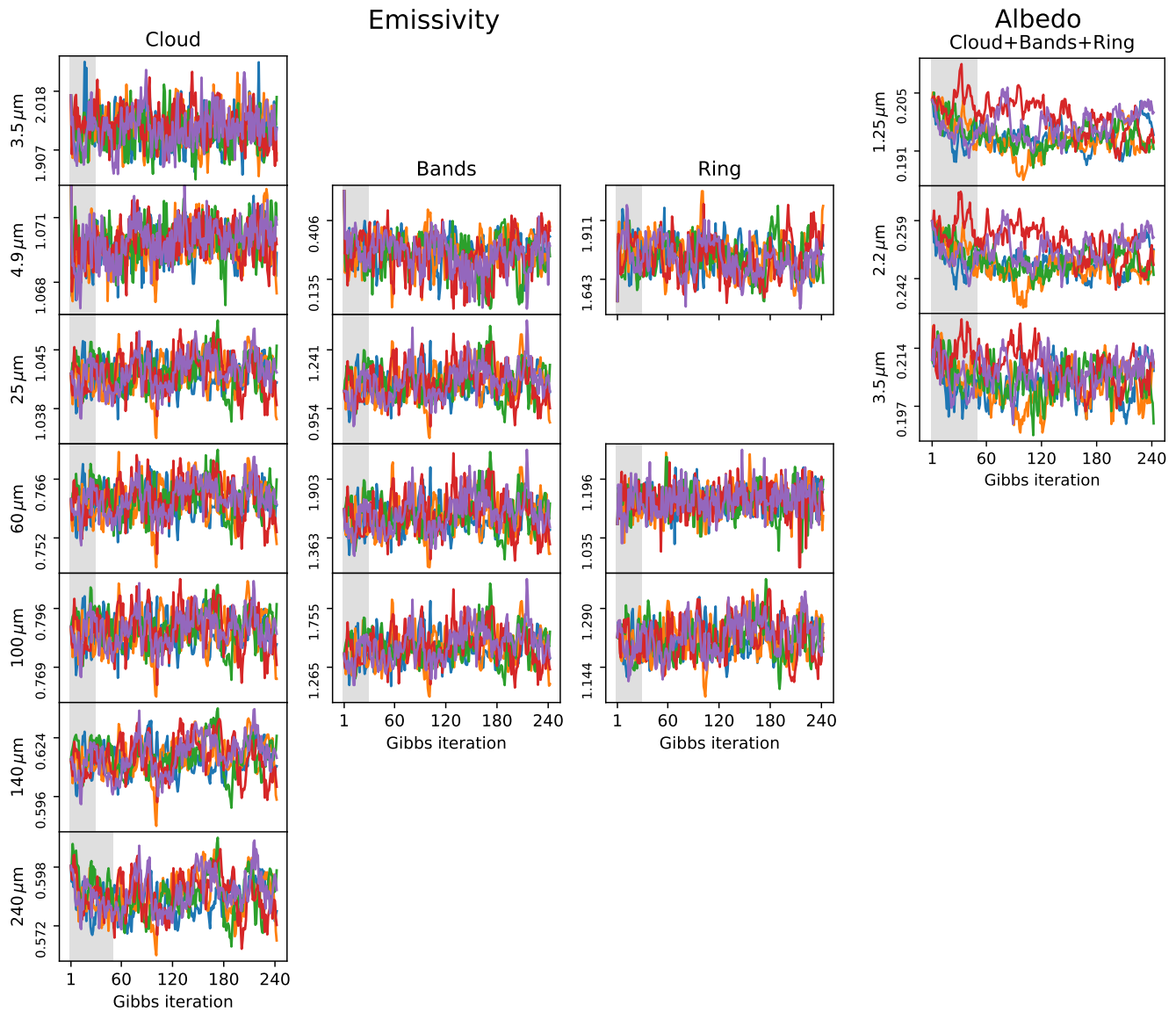


Fig. 8. Trace plots of the wavelength dependent emissivity and albedo parameters. Different colors indicate five independent Markov chains, the gray regions indicate the burn-in set for each parameter, and vertical axes were cropped to emphasize convergence.

match the longest convergence period among all parameters, ensuring that an equal number of post-burn-in samples was used for all correlations. This plot is highly structured, reflecting the complexity of the ZL likelihood. Particularly strong are the correlations between the emissivity parameters in the 60–240 μm channels. As already noted above, fitting a smooth parametric ZL SED function rather than individual amplitude factors at each of these channels should be beneficial in many ways; both in terms of physical interpretation, but also in terms of overall sampling efficiency in a Gibbs sampler.

5.2. Updated ZL model

To estimate the marginal posterior distribution for each ZL parameter individually, we compute the mean and standard deviation of all post-burn-in samples. For each parameter the number of burn-in samples was tuned individually, as shown in Figs. 7 and 8. The resulting values for the shape parameters are tabulated in the fourth column of Table 1, the amplitude

parameters are provided in Table 2, and the phase function parameters can be found in Table 3. For comparison, the corresponding values from Kelsall et al. (1998) and Hong (1985) are listed in the third column in each table. The fifth and final column lists the uniform priors imposed on each parameter in the DR2 analysis.

In general, we see that the differences between DR2 and K98 vary for many more parameters than predicted by the reported statistical uncertainties. For instance, the density parameters of dust bands 1 and 2 are approximately 67 % and 25 % lower in the DR2 model than in K98. However, at frequencies below 140 μm , the emissivities of all components are higher in DR2 than in K98, which compensates for the lower densities and results in a similar total intensity. Figure A.3 in Appendix A compares the mission-averaged ZL maps for both models per component. Here we see visually that in the DR2 maps both the smooth cloud and the three dust bands are fainter than in the K98 maps. The intensity of the third asteroidal band is particularly weak in our model but, as already noted, we can

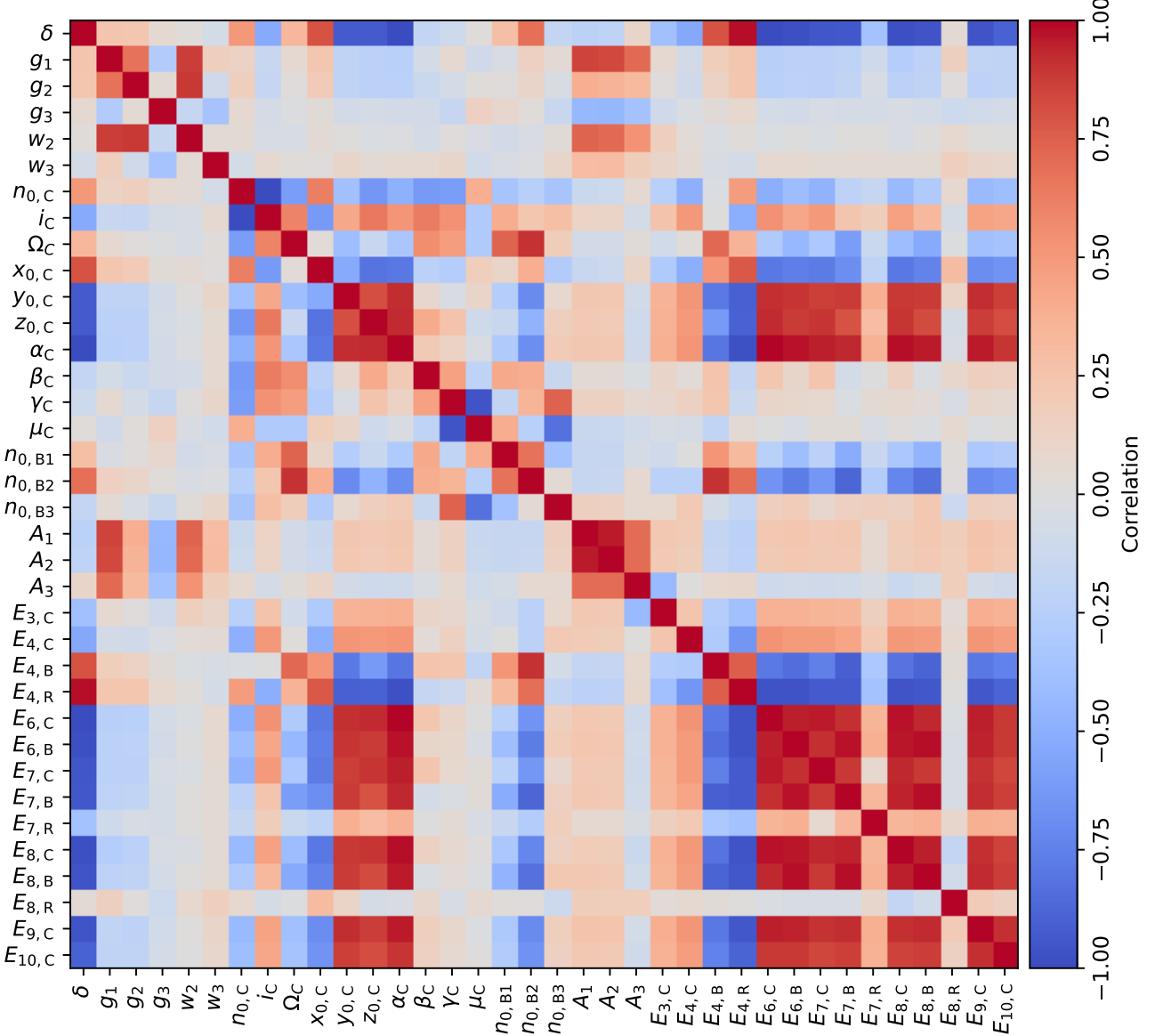


Fig. 9. Correlations between the fitted ZL parameters ζ_z .

915 not conclude that we have a detection of it with the DIRBE
916 data alone.

917 As it is the main difference between the K98 and the
918 DR2 ZL models, Figure 10 shows the phase function $\Phi(\Theta)$
919 as defined in Kelsall et al. (1998) (red lines), in Hong (1985)
920 (black dashed line) and in this paper (black solid line). All
921 the models are normalized over the interval $\Theta \in [65^\circ, 125^\circ]$,
922 since this is the interval of solar elongation angle that DIRBE
923 is able to observe. The DR2 phase function was obtained
924 by computing the average and the standard deviation of all
925 phase function values resulting from post-burn-in parame-
926 ters.

927 Figure 11 compares the predicted ZL intensity as a function
928 of wavelength for three different positions on the sky at one given
929 day in different colors, as well as the average over the full sky
930 in black. Solid and dashed lines show the DR2 and K98 predic-
931 tions, respectively. The bottom panel shows the relative differ-
932 ence. In general, the two models agree to better than 10 % for

933 most wavelengths, except at the very longest, for which the
934 overall amplitudes are very uncertain.

935 Figure 12 shows a similar relative difference, but now as a
936 function of position on the sky for the 12 and 25 μm channels.
937 In these channels, for which the ZL emission is the brightest, the
938 K98 and COSMOGLOBE DR2 models agree to within $\lesssim 3\%$ over
939 most of the sky. These differences are thus similar in magnitude
940 to the relative residuals measured by Kelsall et al. (1998), which
941 were found to be $\sim 2\%$ at 12 μm .

5.3. Goodness-of-fit

This whole subsection needs to be revised

944 Next, we consider the absolute goodness-of-fit of the Cos-
945 MOGLOBE DR2 model, and we start by inspecting the half-mission
946 data-minus-model residual maps for each channel, which are
947 shown in Fig. 13. We note that these maps show total residu-
948 als, and therefore include contributions from ZL, Galactic fore-
949 grounds, and instrumental noise.

Table 1. Best-fit interplanetary dust parameter estimates and uncertainties in the DR2 analysis, comparing values with the K98 model. Parameters that are not listed are fixed at the respective K98 values.

| Parameter | Description | K98 | DR2 | Uniform prior |
|---|--|---------------|---------------|---------------------------------------|
| Smooth Cloud | | | | |
| $n_{0,C}$ [10 ⁻⁸ AU ⁻¹] | Number density at 1 AU | 11.3 ± 0.1 | 10.56 ± 0.03 | [10 ⁻³ , 10 ³] |
| α | Radial power-law exponent | 1.34 ± 0.02 | 1.34 ± 0.04 | [1, 2] |
| β | Vertical shape parameter | 4.14 ± 0.07 | 3.84 ± 0.01 | [3, 5] |
| γ | Vertical power-law exponent | 0.94 ± 0.03 | 0.91 ± 0.02 | [0.3, 1.1] |
| μ | Widening parameter | 0.189 ± 0.014 | 0.223 ± 0.009 | [0.1, 0.4] |
| i [deg] | Inclination | 2.03 ± 0.02 | 2.195 ± 0.007 | [-30, 30] |
| Ω [deg] | Ascending node | 77.7 ± 0.6 | 75.6 ± 0.1 | [-720, 720] |
| x_0 [10 ⁻² AU] | x-offset from the Sun | 1.2 ± 0.1 | 0.57 ± 0.02 | [-4, 4] |
| y_0 [10 ⁻² AU] | y-offset from the Sun | 0.55 ± 0.8 | -0.56 ± 0.02 | [-2, 2] |
| z_0 [10 ⁻³ AU] | z-offset from the Sun | -2.2 ± 0.4 | -0.71 ± 0.02 | [-20, 20] |
| Dust bands | | | | |
| n_{0,B_1} [10 ⁻¹⁰ AU ⁻¹] | Number density at 1 AU for dust band 1 | 5.6 ± 0.7 | 1.8 ± 0.2 | [0.1, 10 ⁵] |
| n_{0,B_2} [10 ⁻⁹ AU ⁻¹] | Number density at 1 AU for dust band 2 | 1.99 ± 0.13 | 1.49 ± 0.10 | [0.1, 10 ⁵] |
| n_{0,B_3} [10 ⁻¹⁰ AU ⁻¹] | Number density at 1 AU for dust band 3 | 1.4 ± 0.2 | < 0.32 | [0.1, 10 ⁵] |

Starting with the near-infrared 1.25–3.5 μm channels, we see that these are primarily dominated by residual starlight emission, seen in the form of the bright Galactic plane and the scattered points source residuals at high Galactic latitudes. However, sub-dominant contributions from ZL residuals are also clearly seen in the form of diffuse structures aligned with the Ecliptic plane and poles. For instance, in the 1.25 μm first half-mission map, denoted by HM1, which corresponding to the first five months of the mission, we see a faint band with alternating sign that follows the Ecliptic plane. In fact, similar features may be seen in all channels below 100 μm , and future work should clearly aim at establishing a more detailed model of ZL in the Ecliptic plane; again, joint analysis with high-resolution measurements from *IRAS* and *AKARI* should prove extremely useful for this.

In the 1.25 μm HM1 map, we also see a diffuse excess about 45° south-west of the Galactic center, corresponding to the beginning of the DIRBE observing period. On the opposite side of the missing pixel mask, there is a slight deficit. As noted in Sect. 4, we remove the first week of observations to suppress this effect. Similarly, in the HM2 map we note that masked pixels correspond to the last two weeks of the mission, and the residuals change sign on each of the two sides of this masked region. In fact, based on these post-analysis residuals, it appears that it might be worth considering removing a few more days at either end of the survey to remove even more of these residuals. Of course, it is impossible to determine from this analysis alone whether these observed residual are due to real ZL variations or instrumental drifts. However, the fact that more than 90 % of the survey appears free of sharp edges, and the main features appear either at the end or beginning of the survey suggests at least that an instrumental origin cannot be excluded a priori. For the 4.9–100 μm channels, a whole month is removed at the end of the survey, and a corresponding larger region of missing pixels is seen in HM2.

At 4.9 μm , a peculiar hot band is seen in the south-western quadrant that is close to, but not actually aligned with, the Ecliptic

plane. A corresponding blue swath may be seen normal to the Galactic plane in the eastern quadrant. This feature is discussed by Watts et al. (2024a), and shown to correlate directly with a bright feature in excess solar-centric coordinates. Future studies should consider whether this could be explained in terms of stray-light emission, and, if it cannot, then the parametric ZL model for the circumsolar ring and Earth-trailing feature needs to be modified.

Finally, the 100 and 140 μm channels are clearly dominated by Galactic residuals. Any improvement in the ZL model for these channels should therefore be accompanied by corresponding improvements in the thermal dust modeling.

These qualitative observations can be made more quantitative by considering the reduced χ^2 , as optimized within the parameter estimation algorithm. The best-fit χ^2_{red} values are reported for each channel in the rightmost column of Table 4; note that the 1.25–3.5 μm and the 12–60 μm channels are processed jointly when fitting the parameters, and χ^2_{red} is therefore only properly defined for the two groups. For completeness, the second column lists the number of TOD samples used to fit the ZL parameters, and the third column lists the instrumental white noise rms per TOD sample.

For ideal data, with a perfectly fitting model, we would expect $\chi^2_{\text{red}} \sim 1$, with a standard deviation given by $\sqrt{2/N_{\text{samp}}} \sim 0.005$. Clearly, the current model is not a perfect match to the observed data, and significant deviations are observed. Still, the values are for several channels very close to unity, namely **140** and **240 μm** .

The biggest outliers are the 12–60 μm channels, which have the highest signal-to-noise ratio to ZL emission. In this case, the reduced χ^2 is **2.17**, which indicates that the white noise rms accounts for only about 40 % of the total variation seen in the residual TOD; the rest is most naturally explained in terms of ZL modeling errors. However, in this respect it is worth noting that our estimates of the noise level, as reported by Watts et al. (2024a), are significantly lower than those used

Table 2. Best-fit estimates and uncertainties of the source-function parameters in the DR2 analysis, comparing values with the K98 model. Parameters that are not listed are fixed at the respective K98 values.

| Parameter | Description | K98 | DR2 | Uniform prior |
|---------------------------|---------------------------------|-----------------------------|----------------------|---------------|
| All zodiacal components | | | | |
| δ | Temperature power-law exponent | 0.467 ± 0.004 | 0.406 ± 0.009 | [0.3, 0.5] |
| A_1 | Albedo at $1.25\mu\text{m}$ | 0.204 ± 0.001 | 0.195 ± 0.004 | [0, 1] |
| A_2 | Albedo at $2.2\mu\text{m}$ | 0.255 ± 0.002 | 0.248 ± 0.005 | [0, 1] |
| A_3 | Albedo at $3.5\mu\text{m}$ | 0.21 ± 0.02 | 0.205 ± 0.006 | [0, 1] |
| Smooth Cloud | | | | |
| E_1 | Emissivity at $1.25\mu\text{m}$ | 1 Fixed | 1 Fixed | |
| E_2 | Emissivity at $2.2\mu\text{m}$ | 1 Fixed | 1 Fixed | |
| E_3 | Emissivity at $3.5\mu\text{m}$ | 1.66 ± 0.09 | 1.95 ± 0.03 | [0, 10] |
| E_4 | Emissivity at $4.9\mu\text{m}$ | 0.997 ± 0.004 | 1.070 ± 0.001 | [0, 10] |
| E_5 | Emissivity at $12\mu\text{m}$ | 0.958 ± 0.003 | 1 Fixed | |
| E_6 | Emissivity at $25\mu\text{m}$ | 1 Fixed | 1.042 ± 0.002 | [0, 10] |
| E_7 | Emissivity at $60\mu\text{m}$ | 0.733 ± 0.006 | 0.761 ± 0.004 | [0, 10] |
| E_8 | Emissivity at $100\mu\text{m}$ | 0.647 ± 0.012 | 0.786 ± 0.008 | [0, 10] |
| E_9 | Emissivity at $140\mu\text{m}$ | 0.677 | 0.615 ± 0.008 | [0, 10] |
| E_{10} | Emissivity at $240\mu\text{m}$ | 0.519 | 0.586 ± 0.008 | [0, 10] |
| Dust bands | | | | |
| E_1 | Emissivity at $1.25\mu\text{m}$ | 1 Fixed | 1 Fixed | |
| E_2 | Emissivity at $2.2\mu\text{m}$ | 1 Fixed | 1 Fixed | |
| E_3 | Emissivity at $3.5\mu\text{m}$ | 1.66 Fixed to cloud | 1.92 Fixed to cloud | |
| E_4 | Emissivity at $4.9\mu\text{m}$ | 0.36 ± 0.05 | 0.25 ± 0.08 | [0, 10] |
| E_5 | Emissivity at $12\mu\text{m}$ | 1.0 ± 0.2 | 1 Fixed | |
| E_6 | Emissivity at $25\mu\text{m}$ | 1 Fixed | 1.09 ± 0.08 | [0, 10] |
| E_7 | Emissivity at $60\mu\text{m}$ | 1.3 ± 0.3 | 1.6 ± 0.2 | [0, 10] |
| E_8 | Emissivity at $100\mu\text{m}$ | 1.5 ± 0.65 | 1.4 ± 0.1 | [0, 10] |
| E_9 | Emissivity at $140\mu\text{m}$ | 1.13 | 0.601 Fixed to cloud | |
| E_{10} | Emissivity at $240\mu\text{m}$ | 1.40 | 0.58 Fixed to cloud | |
| Ring and Trailing Feature | | | | |
| E_1 | Emissivity at $1.25\mu\text{m}$ | 1 Fixed | 1 Fixed | |
| E_2 | Emissivity at $2.2\mu\text{m}$ | 1 Fixed | 1 Fixed | |
| E_3 | Emissivity at $3.5\mu\text{m}$ | 1.66 Fixed to cloud | 1.92 Fixed to cloud | |
| E_4 | Emissivity at $4.9\mu\text{m}$ | 1.06 ± 0.09 | 1.74 ± 0.08 | [0, 10] |
| E_5 | Emissivity at $12\mu\text{m}$ | 1.06 ± 0.01 | 1 Fixed | |
| E_6 | Emissivity at $25\mu\text{m}$ | 1 Fixed | 1 Fixed | |
| E_7 | Emissivity at $60\mu\text{m}$ | 0.873 ± 0.004 | 1.14 ± 0.04 | [0, 10] |
| E_8 | Emissivity at $100\mu\text{m}$ | $1.10 \pm 7 \times 10^{-6}$ | 1.22 ± 0.04 | [0, 10] |
| E_9 | Emissivity at $140\mu\text{m}$ | 1.13 | 0.601 Fixed to cloud | |
| E_{10} | Emissivity at $240\mu\text{m}$ | 1.40 | 0.58 Fixed to cloud | |

1022 for previous ZL analysis with DIRBE observations. For instance,
 1023 Rowan-Robinson & May (2013) adopted uncertainties of 0.80
 1024 and 0.93 MJy/sr per sample at 12 and $25\mu\text{m}$, respectively, which
 1025 are 8 and 5 times larger than our estimates. Despite assuming

such large uncertainties, they obtained a reduced χ^2 of 1.30 with 1026 their extended model. In contrast, if we had adopted the same 1027 white noise estimates, we would have obtained a reduced χ^2 of 1028 ~ 0.1 , which immediately would suggest significant noise rms 1029

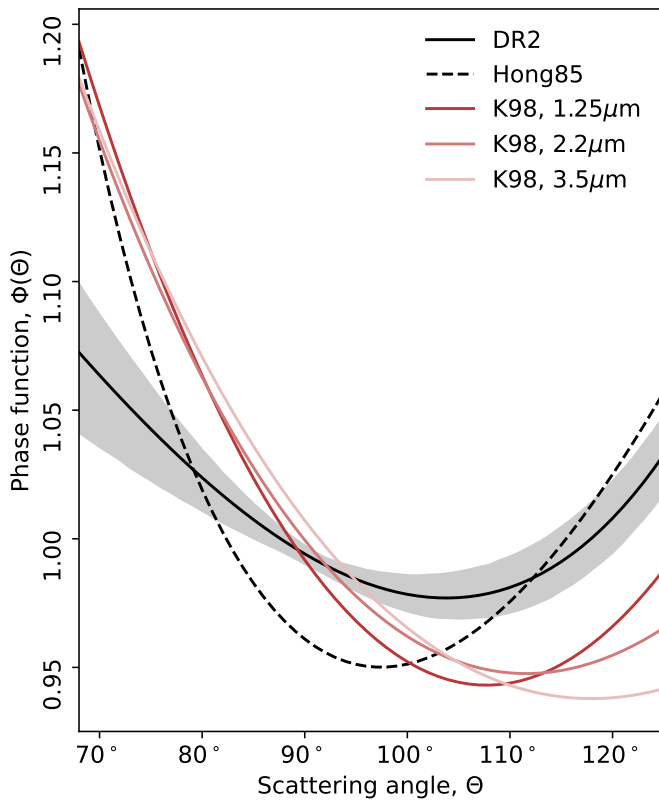


Fig. 10. Comparison of different parametrizations of the phase function $\Phi(\Theta)$, normalized over the solar elongation angle interval observed by DIRBE ($\Theta \in [65^\circ, 125^\circ]$). The red lines represent $\Phi(\Theta)$ as defined by the original K98 model (Kelsall et al. 1998) in the frequency channels $1.25 - 3.5 \mu\text{m}$; the black dashed line is the phase function defined in Hong (1985); while the solid black line is the DR2 function. This final one follows the definition of Equation 15 and uses all the post-burn-in parameters to obtain the mean value and the standard deviation of Φ , shown as a line and a grey area respectively in the figure.

Table 3. Best-fit phase function parameter estimates and uncertainties in the DR2 analysis, comparing values with those listed in Hong (1985).

| Parameter | Hong | DR2 | Uniform prior |
|-------------------|-------|------------------------------|---------------|
| Asymmetry factors | | | |
| $g_1 \dots \dots$ | 0.70 | 0.09 ± 0.03 | $[-1, 1]$ |
| $g_2 \dots \dots$ | -0.20 | -0.47 ± 0.05 | $[-1, 1]$ |
| $g_3 \dots \dots$ | -0.81 | -0.86 ± 0.09 | $[-1, 1]$ |
| Weights | | | |
| $w_2 \dots \dots$ | 0.330 | 0.18 ± 0.03 | $[0, 1]$ |
| $w_3 \dots \dots$ | 0.005 | $0.005 \pm 1 \times 10^{-5}$ | $[0, 1]$ |

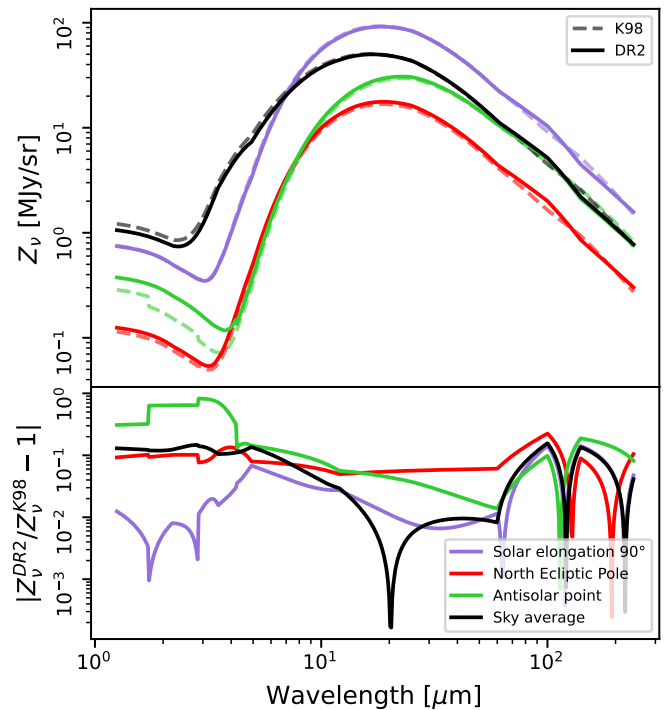


Fig. 11. (Top panel:) ZL intensity as a function of wavelength on the 2024-01-01 as predicted by the DR2 (solid lines) and K98 (dashed lines) models. Colors show three different positions on the sky with Galactic coordinates ($l = 39.91^\circ, b = -58.70^\circ$), ($l = 96.38^\circ, b = 29.81^\circ$), and ($l = 191.41^\circ, b = 8.68^\circ$) corresponding to the solar elongation at 90° , the north ecliptic pole, and the antisolar point, respectively. The black curves instead show the full-sky average. (Bottom:) Fractional difference between the DR2 and 98 models, evaluated from the results shown in the top panel.

Table 4. Reduced goodness-of-fit (χ_{red}^2) values for one arbitrarily selected Gibbs sample, along with the number of TOD samples used to fit the ZL parameters (N_{samp}) and the instrument white noise rms per 8 Hz sample for each DIRBE channel (σ_0). Note that the $1.25 - 3.5 \mu\text{m}$ and the $12 - 60 \mu\text{m}$ channels are analyzed jointly; therefore, the values of N_{samp} and χ_{red}^2 refer to the combined groups.

| λ (μm) | N_{samp} | σ_0 [MJy/sr] | χ_{red}^2 |
|----------------|-------------------|---------------------|-----------------------|
| 1.25 | 668 | 0.022 | 1.11 |
| 2.2 | ... | 0.024 | ... |
| 3.5 | ... | 0.023 | ... |
| 4.9 | 118 | 0.028 | 1.19 |
| 12 | 2052 | 0.109 | 2.17 |
| 25 | ... | 0.209 | ... |
| 60 | ... | 0.369 | ... |
| 100 | 122 | 0.417 | 1.91 |
| 140 | 31 | 32.030 | 1.02 |
| 240 | 35 | 18.042 | 1.03 |

1030 over-estimation. In other words, the current COSMOGLOBE DR2
1031 analysis has resulted both in significantly lower white noise un-
1032 certainties and lower absolute residuals for the main ZL chan-
1033 nels.

1034 At the same time, we do in fact obtain reduced χ^2 values that
1035 are lower than unity at the two shortest wavelengths. These val-
1036 ues suggest that our noise estimates at 1.25 and $2.2 \mu\text{m}$ are over-

estimated by about 15 %. The origin of this discrepancy should 1037 be identified and mitigated in future analyses, and it will then be 1038 natural to consider the effect of the highly asymmetric beam re- 1039 sponse of the DIRBE instrument, coupled to the strong starlight 1040 emission at these channels. In the current analysis, we assume 1041 that the DIRBE beams are azimuthally symmetric (Watts et al. 1042 2024a), and residuals due to that assumption could presumably 1043 easily bias the noise estimates by 15 %. 1044

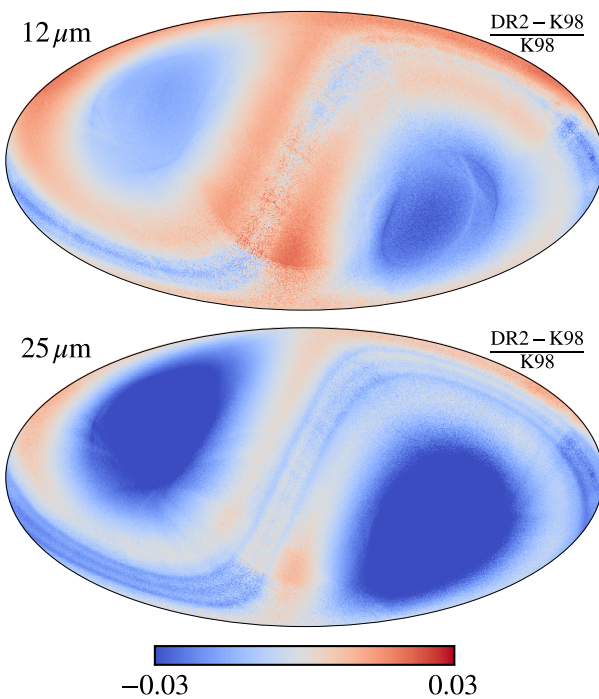


Fig. 12. Relative fractional difference between mission averaged ZL simulations of our best-fit model and K98 at 12 and 25 μm . To highlight structural zodiacal light differences, an estimate value of the ZL monopole (as evaluated in Fig. 16) was subtracted from the DR2 model in both channels before the comparison was carried out.

1045 5.4. Comparison of ZSMA maps

1046 A primary goal of the parametric ZL model presented here is
1047 to establish a set of zodiacal light subtracted mission averaged
1048 (ZSMA) frequency maps for each DIRBE channel that can be
1049 used for cosmological and astrophysical analysis. These maps
1050 are simply derived by subtracting the ZL component from the
1051 TOD, and bin the rest into pixelized sky maps.

1052 Figures 14 and 15 compare the K98 ZSMA maps (second column)
1053 with the new COSMOGLOBE DR2 ZSMA maps (third column),
1054 as well as with the corresponding non-ZL-subtracted maps
1055 (first column). **The 12–60 μm DR2 ZSMA maps present negative values along the Ecliptic plane, indicating that the actual zodiacal light signal is lower than what is predicted by the model in use.** Despite this, here we clearly see that the COSMOGLOBE approach results in significantly lower ZL residuals at all channels below 140 μm , while for the two longest wavelength channels the two maps appear visually very similar. The improvements are particularly striking between 4.9 and 60 μm : in this frequency range zodiacal emission is the strongest, yet the DR2 ZSMA maps are for the first time dominated by Galactic signal at high latitudes rather than by ZL residuals. In summary, even though further work is needed to address the over-subtraction in channels 12–60 μm , this analysis represents a significant advance in zodiacal light modeling for DIRBE, particularly in the mid-infrared.

1071 One of the primary scientific goals of the entire DIRBE ex-
1072 periment was to measure the CIB monopole spectrum, which es-
1073 sentially corresponds to the zero-level of the ZSMA maps shown
1074 in Figs. 14 and 15. It is therefore of great interest to measure
1075 the difference in zero-levels between the K98 and DR2 maps,

1076 shown in Fig. 16 for the 1.25–25 μm channels, evaluated out-
1077 side the same confidence masks as described in Sect. 4.2. For reference, the best-fit theoretical model of Fink et al. (2022) is plotted as a dotted line. First, we note that the difference is defined as K98-minus-DR2, which is always positive. In other words, the new analysis appears to have removed more ZL than the K98 analysis. In fact, the measured monopole difference is actually also higher than the theoretical CIB monopole spectrum itself, suggesting that the modifications are in fact $O(1)$ or larger as measured relatively to the main science target of DIRBE; at 12 and 25 μm , the differences are almost two orders of magnitude. For further discussion regarding the scientific implications of these differences in terms of the CIB monopole, we refer the interested reader to Watts et al. (2024b).

1089 Figure 17 shows the results from a similar calculations, but this time in the form of the rms ratio of the ZSMA maps evaluated outside the same masks. **Here we see that the DR2 maps have lower rms than the K98 maps in all the channels between 1.25 and 25 μm , which once again indicates that more ZL emission has been removed from the new maps.**

6. Conclusions

We have presented a new Bayesian framework for modeling zodiacal light from time-ordered observations, and applied this to the DIRBE experiment. We find that the resulting ZL model differs significantly from the K98 model, both in terms of mean parameter values and uncertainties, and the new model results in much cleaner ZL-subtracted frequency maps. We strongly recommend that any future cosmological or astrophysical analysis that involves DIRBE frequency maps should use the COSMOGLOBE DR2 maps.

These large improvements stem from two foundational features of the COSMOGLOBE framework. First, the new analysis used external observations from *Planck*, WISE and *Gaia* to model Galactic signals, and thereby break, or at least minimize, over-all parameter degeneracies. Second, the current framework fits all parameters simultaneously, both those of astrophysical and instrumental nature. This is achieved through a process called Gibbs sampling, which maps out the full joint posterior distribution by iterating through a large number of conditional distributions.

While this Gibbs sampling approach is a key ingredient in the global process, and it is difficult to envision how the full framework would work without it, this method is also associated with significant numerical challenges. In particular, it is well known that Gibbs sampling struggles with probing strongly degenerate distributions, and the ZL posterior distribution in question in this paper is precisely that. Furthermore, this distribution does not only exhibit strong degeneracies, but also a huge number of local extrema in which a Markov chain can easily get trapped.

Another issue regarding the current model is physical plausibility. In this first application of the Bayesian end-to-end framework, an important goal was to understand how well the current data constrains the parametric model. As a result, only weak uniform priors are imposed on the main fitted parameters. On the one hand, this does ensure that the final residuals are minimized, which is good for astrophysical and cosmological applications of the resulting ZSMA maps – but it also means that some parameters may have likely drifted into non-physical parameter values.

Overcoming all of these challenges will most likely involve at least two main tasks. First, by analyzing additional and complementary data, for instance from high-resolution experiments such as *AKARI* and *IRAS* jointly with the DIRBE measurements,

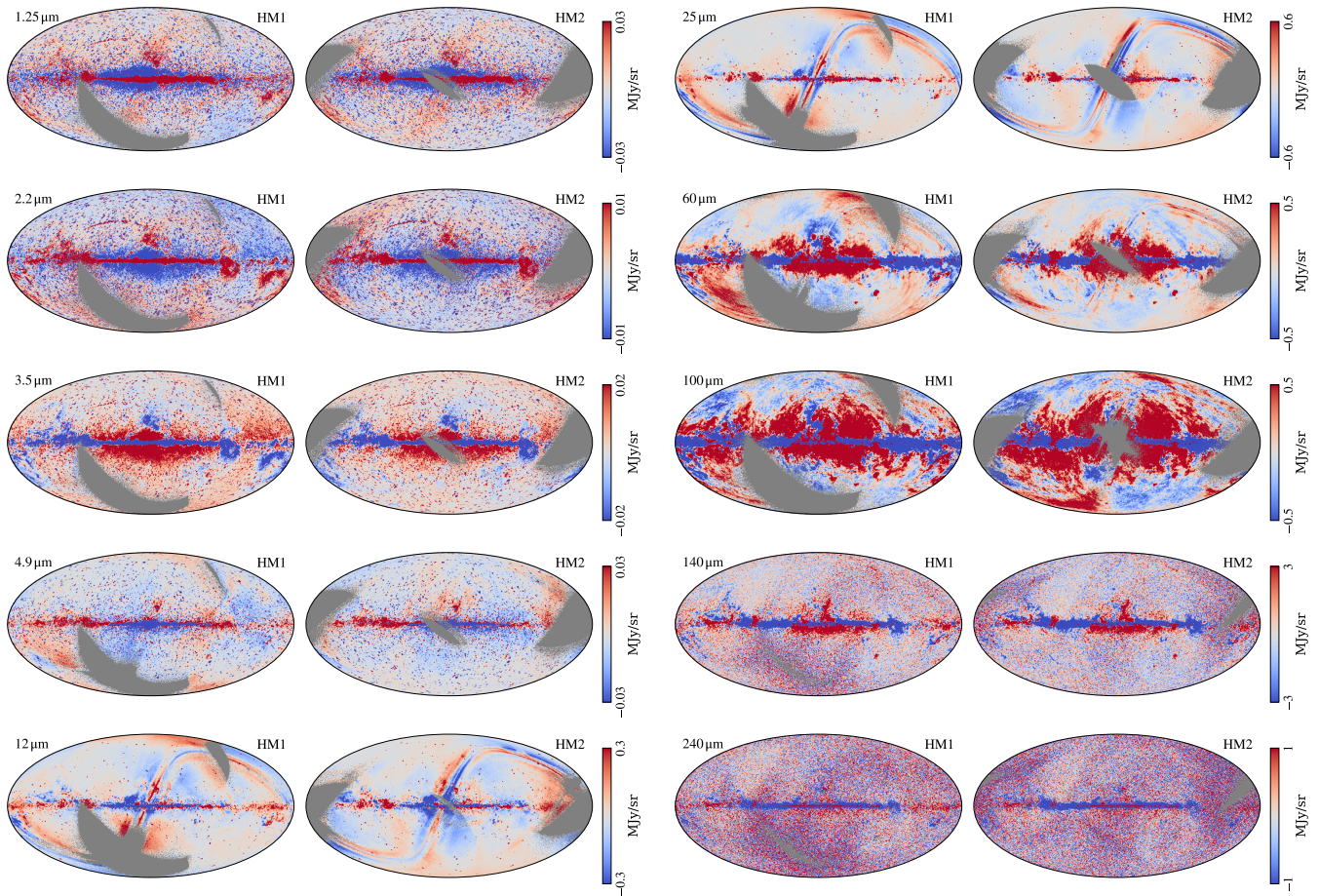


Fig. 13. Half-mission data-minus-signal residual maps for each channel. The two columns within each wavelength section correspond to the first (HM1) and second (HM2) half-mission maps, respectively. All bands between 1.25 and $100\,\mu\text{m}$ have been smoothed with a $15'$ Gaussian kernel, and the 140 and $240\,\mu\text{m}$ channels have been smoothed with a $30'$ FWHM kernel. The gray regions represent unobserved pixels in the half-mission splits.

many of the current strong degeneracies are likely to be effectively broken. In particular the structure of the asteroidal bands, for which DIRBE's low angular resolution is a severe limitation, should become much better probed with these data. Still, even with more data there are likely to be several degeneracies present that are difficult to predict in advance. Implementing better and faster sampling algorithms should therefore be a high-priority topic for future work, for instance using ideas from simulated annealing and/or Hamiltonian sampling. **Furthermore, future analyses will also include SPHEREx data, which will allow testing of the ZL model at wavelengths closer to the visible and contribute to ongoing efforts toward developing an optical zodiacal light model (e.g., O'Brien et al. (2025)).**

In addition, it is by no means obvious that a low-dimensional 3D model such as K98 with only $O(10^2)$ free parameters can describe such a rich and dynamical system as ZL to the required precision for next-generation cosmology. Future work should therefore also consider conceptual generalizations of the entire framework. One step in this direction was taken by Rowan-Robinson & May (2013), who introduced a different set of basis components than K98; indeed, the new fit presented in this paper appears to have moved toward that model within the K98 framework. More drastic approaches would be to consider perturbative Taylor expansion models around the existing components, or even fully voxelized 3D models. Obviously, these would be highly degenerate when using only near-Earth observations, but

perhaps in combination with data from solar system probes such as Juno or New Horizons, new insights may be gained.

In conclusion, it is clear that the ZL model presented in this paper suffers from many shortcomings of both modeling and algorithmic origin, and these must be addressed through future extensions of the COSMOGLOBE framework. At the same time, and despite all these shortcomings, it is equally clear that this model redefines the state-of-the-art of ZL modeling for the DIRBE data, reducing residuals by orders of magnitude in the mid-infrared regime. Furthermore, this work has established an effective computational framework that can be extended to other data sets with relatively minor effort, and that will allow equally large steps forward to be made. All in all, this work has established a new reference for the analysis of past, present and future infrared experiments, building directly on a long line of algorithmic breakthroughs initially developed for the CMB field.

Acknowledgements. We thank Tony Banday, Johannes Eskilt, Dale Fixsen, Ken Ganga, Paul Goldsmith, Shuji Matsuura, Sven Wedemeyer, and Janet Weiland for useful suggestions and guidance. The current work has received funding from the European Union's Horizon 2020 research and innovation programme under grant agreement numbers 819478 (ERC; COSMOGLOBE; bit2cosmology), 101165647 (ERC; ORIGINS), 101141621 (ERC; COMMANDER; and 101007633 (MSCA; CMBINFLATE). This research is also funded by the Research Council of Norway under grant agreement number 344934 (YRT; COSMOGLOBEHD). Some of the results in this paper have been derived using healpy (Zonca et al. 2019) and the HEALPix (Górski et al. 2005) packages. We acknowledge the use of the Legacy Archive for Microwave Background Data Analysis (LAMBDA), part of the High Energy Astrophysics Science Archive

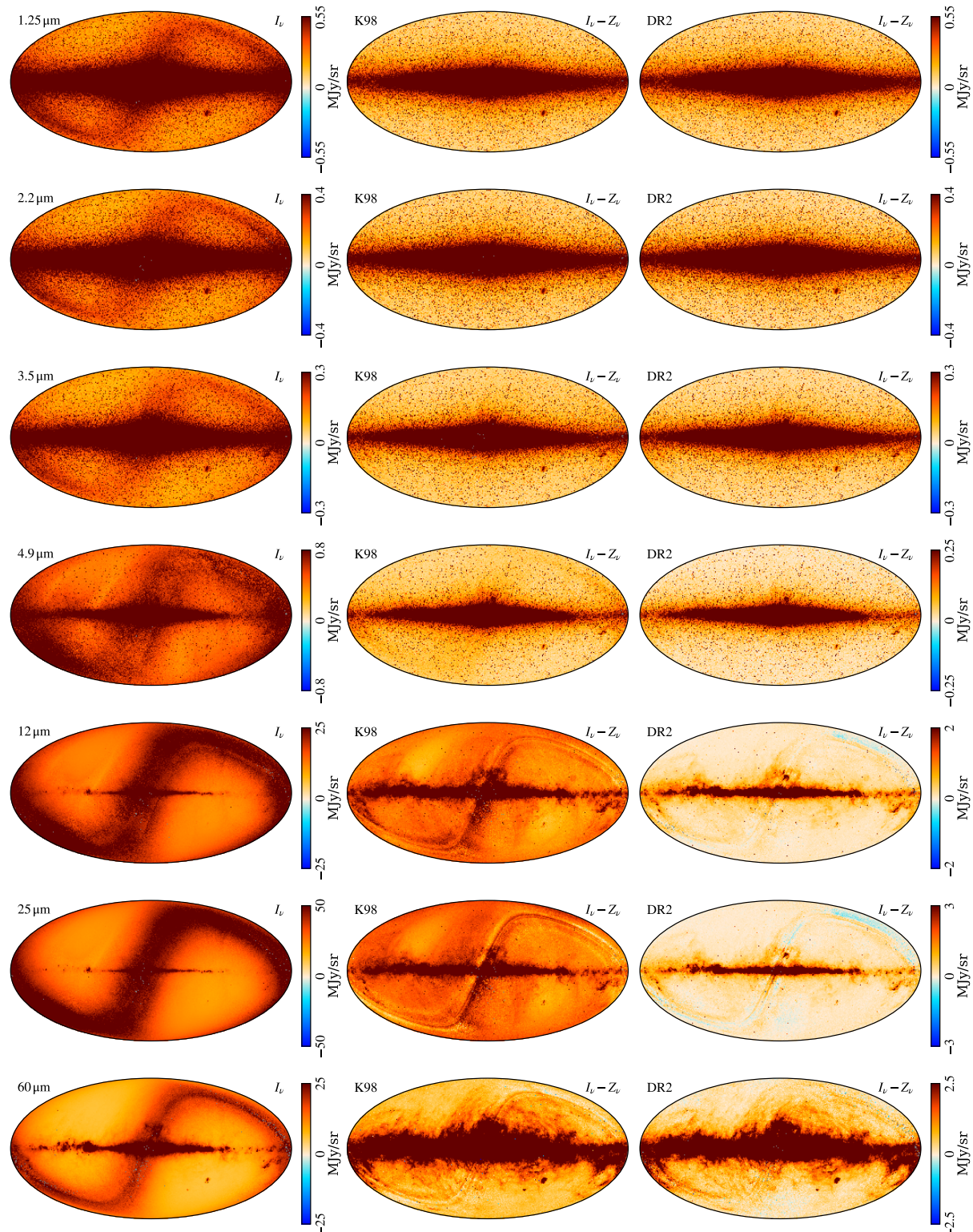


Fig. 14. (Left column): Mission-averaged frequency maps containing ZL after data selection. **(Middle column):** DIRBE ZSMA maps. **(right column):** Our ZL subtracted mission-average maps. All the maps are at our native HEALPix resolution of $N_{\text{side}} = 512$. Rows show, from top to bottom, DIRBE channels from 1.25 to 60 μm .

1192 Center (HEASARC). HEASARC/LAMBDA is a service of the Astrophysics
 1193 Science Division at the NASA Goddard Space Flight Center. This publica-
 1194 tion makes use of data products from the Wide-field Infrared Survey Explorer,
 1195 which is a joint project of the University of California, Los Angeles, and the
 1196 Jet Propulsion Laboratory/California Institute of Technology, funded by the
 1197 National Aeronautics and Space Administration. This work has made use of
 1198 data from the European Space Agency (ESA) mission *Gaia* (<https://www.cosmos.esa.int/gaia>).

1199 [cosmos.esa.int/gaia](https://www.cosmos.esa.int/gaia)), processed by the *Gaia* Data Processing and Anal-
 1200 ysis Consortium (DPAC, <https://www.cosmos.esa.int/web/gaia/dpac/>
 1201 consortium). Funding for the DPAC has been provided by national institutions,
 1202 in particular the institutions participating in the *Gaia* Multilateral Agreement.
 1203 We acknowledge the use of data provided by the Centre d'Analyse de Données
 1204 Etendues (CADE), a service of IRAP-UPS/CNRS (<http://cade.irap.omp.eu>, Par-
 1205 adis et al. 2012). This paper and related research have been conducted during
 1206

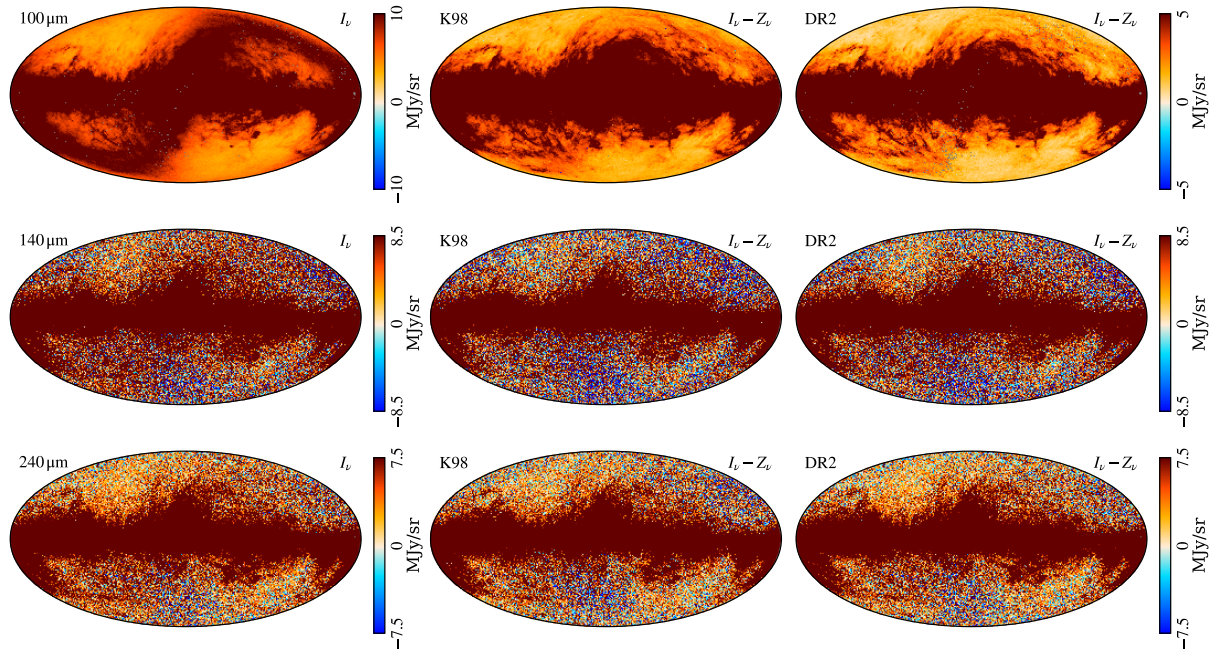


Fig. 15. Same as Fig. 14, but for the 100–240 μm channels.

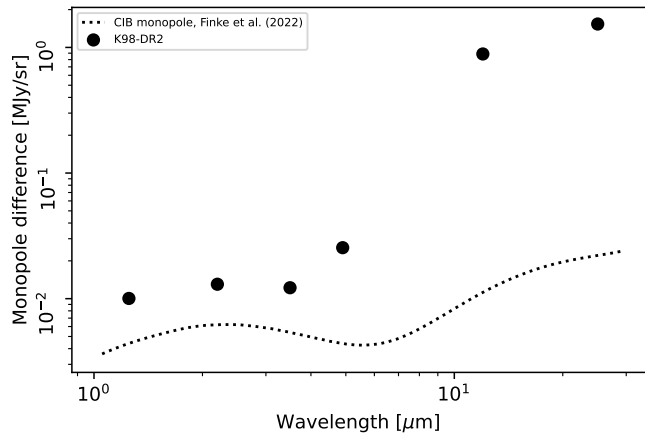


Fig. 16. Monopole difference between the official K98 and COSMOGLOBE DR2 ZSMA maps, evaluated as the average of the difference between the maps at 1.25–25 μm , as shown in the second and third columns of Fig. 14, outside the DR2 analysis masks.

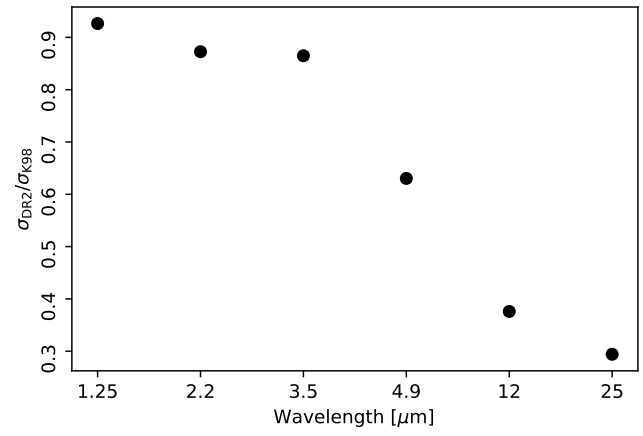


Fig. 17. RMS ratio between the COSMOGLOBE DR2 and K98 ZSMA maps, $\sigma_{\text{DR2}}/\sigma_{\text{K98}}$, as evaluated outside the DR2 analysis masks.

and with the support of the Italian national inter-university PhD programme in Space Science and Technology. Work on this article was produced while attending the PhD program in PhD in Space Science and Technology at the University of Trento, Cycle XXXIX, with the support of a scholarship financed by the Ministerial Decree no. 118 of 2nd March 2023, based on the NRRP - funded by the European Union - NextGenerationEU - Mission 4 "Education and Research", Component 1 "Enhancement of the offer of educational services: from nurseries to universities" - Investment 4.1 "Extension of the number of research doctorates and innovative doctorates for public administration and cultural heritage" - CUP E66E23000110001.

1216 References

- 1217 Arendt, R. G. 2014, AJ, 148, 135
 1218 Arendt, R. G., Odegard, N., Weiland, J. L., et al. 1998, ApJ, 508, 74
 1219 Bennett, C. L., Larson, D., Weiland, J. L., et al. 2013, ApJS, 208, 20
 1220 BeyondPlanck Collaboration, Andersen, K. J., Aurlien, R., et al. 2023, A&A,
 1221 675, A1

| | |
|---|------|
| Carleton, T., Windhorst, R. A., O'Brien, R., et al. 2022, AJ, 164, 170 | 1222 |
| Dermott, S. F., Jayaraman, S., Xu, Y. L., Gustafson, B. rA. S., & Liou, J. C. | 1223 |
| 1994, Nature, 369, 719 | 1224 |
| Dermott, S. F., Nicholson, P. D., Burns, J. A., & Houck, J. R. 1984, Nature, 312, | 1225 |
| 505 | 1226 |
| Dikarev, V. V. & Schwarz, D. J. 2015, A&A, 584, A9 | 1227 |
| Eriksen, H. K., O'Dwyer, I. J., Jewell, J. B., et al. 2004, ApJS, 155, 227 | 1228 |
| Finke, J. D., Ajello, M., Domínguez, A., et al. 2022, ApJ, 941, 33 | 1229 |
| Gaia Collaboration et al. 2016, A&A, 595, A1 | 1230 |
| Galloway, M., Andersen, K. J., Aurlien, R., et al. 2023, A&A, 675, A3 | 1231 |
| Galloway, M. et al. 2026, A&A, in preparation [arXiv:20xx.xxxxx] | 1232 |
| Geman, S. & Geman, D. 1984, IEEE Trans. Pattern Anal. Mach. Intell., 6, 721 | 1233 |
| Gerakakis, S., Brilenkov, M., Ieronymaki, M., et al. 2023, The Open Journal of | 1234 |
| Astrophysics, 6, 10 | 1235 |
| Gjerløw et al. 2026a, A&A, in preparation [arXiv:20xx.xxxxx] | 1236 |
| Gjerløw et al. 2026b, A&A, in preparation [arXiv:20xx.xxxxx] | 1237 |
| Górski, K. M., Hivon, E., Banday, A. J., et al. 2005, ApJ, 622, 759 | 1238 |
| Hauser, M. G., Arendt, R. G., Kelsall, T., et al. 1998, ApJ, 508, 25 | 1239 |
| Hauser, M. G. & Dwek, E. 2001, ARA&A, 39, 249 | 1240 |
| Hong, S. S. 1985, A&A, 146, 67 | 1241 |
| Ipatov, S. I., Kutyrev, A. S., Madsen, G. J., et al. 2008, Icarus, 194, 769 | 1242 |
| Jewell, J., Levin, S., & Anderson, C. H. 2004, ApJ, 609, 1 | 1243 |

- 1244 Jones, M. H., Bewsher, D., & Brown, D. S. 2013, Science, 342, 960
 1245 Jorgensen, J. L., Benn, M., Connerney, J. E. P., et al. 2021, Journal of Geophysical Research (Planets), 126, e06509
 1246 Kelsall, T., Weiland, J. L., Franz, B. A., et al. 1998, ApJ, 508, 44
 1247 Kennedy, G. M., Wyatt, M. C., Su, K. Y. L., & Stansberry, J. A. 2011, MNRAS, 417, 2281
 1248 Korngut, P. M., Kim, M. G., Arai, T., et al. 2022, ApJ, 926, 133
 1249 Leinert, C., Bowyer, S., Haikala, L. K., et al. 1998a, A&AS, 127, 1
 1250 Leinert, C., Bowyer, S., Haikala, L. K., et al. 1998b, A&AS, 127, 1
 1251 Leinert, C. & Pitz, E. 1989, A&A, 210, 399
 1252 Liou, J. C., Dermott, S. F., & Xu, Y. L. 1995, Planet. Space Sci., 43, 717
 1253 Low, F. J., Beintema, D. A., Gautier, T. N., et al. 1984, ApJ, 278, L19
 1254 Mann, I., Nakamura, A. M., & Mukai, T. 2009, Small Bodies in Planetary Systems, Vol. 758 (Springer Berlin Heidelberg)
 1255 Neugebauer, G., Habing, H. J., van Duinen, R., et al. 1984, ApJ, 278, L1
 1256 Nieto, M. M., Turyshev, S. G., & Anderson, J. D. 2005, Physics Letters B, 613, 11
 1257 O'Brien, R., Arendt, R. G., Windhorst, R. A., et al. 2025, arXiv e-prints, arXiv:2510.18231
 1258 Paradis, D., Dobashi, K., Shimoikura, T., et al. 2012, A&A, 543, A103
 1259 Partridge, R. B. & Peebles, P. J. E. 1967, ApJ, 148, 377
 1260 Planck Collaboration II. 2020, A&A, 641, A2
 1261 Planck Collaboration III. 2020, A&A, 641, A3
 1262 Poppe, A. R., Lisse, C. M., Piquette, M., et al. 2019, ApJ, 881, L12
 1263 Reach, W. T., Franz, B. A., & Weiland, J. L. 1997, Icarus, 127, 461
 1264 Rigley, J. K. & Wyatt, M. C. 2022, MNRAS, 510, 834
 1265 Rowan-Robinson, M. & May, B. 2013, MNRAS, 429, 2894
 1266 San, M. 2024, Journal of Open Source Software, 9, 6648
 1267 San, M., Herman, D., Erikstad, G. B., Galloway, M., & Watts, D. 2022, A&A, 666, A107
 1268 Sano, K., Matsuura, S., Yomo, K., & Takahashi, A. 2020, ApJ, 901, 112
 1269 Spiesman, W. J., Hauser, M. G., Kelsall, T., et al. 1995, ApJ, 442, 662
 1270 Stenborg, G., Stauffer, J. R., & Howard, R. A. 2018, ApJ, 868, 74
 1271 Sullivan et al. 2026, A&A, in preparation [arXiv:20xx.xxxxx]
 1272 Szalay, J. R., Pokorný, P., Bale, S. D., et al. 2020, ApJS, 246, 27
 1273 Takimoto, K., Arai, T., Matsuura, S., et al. 2022, ApJ, 926, 6
 1274 Takimoto, K., Matsuura, S., Sano, K., & Feder, R. M. 2023, ApJ, 944, 229
 1275 Wandelt, B. D., Larson, D. L., & Lakshminarayanan, A. 2004, Phys. Rev. D, 70, 083511
 1276 Watts, D., Galloway, M., Gjerlow, E., et al. 2024a, A&A, submitted [arXiv:2408.10952]
 1277 Watts, D. et al. 2024b, A&A, in preparation [arXiv:2406.01491]
 1278 Watts, D. J., Basyrov, A., Eskilt, J. R., et al. 2023, A&A, 679, A143
 1279 Wright, E. L., Eisenhardt, P. R. M., Mainzer, A. K., et al. 2010, AJ, 140, 1868
 1280 Zonca, A., Singer, L., Lenz, D., et al. 2019, Journal of Open Source Software, 4, 1298
 1281 1282 1283 1284 1285 1286 1287 1288 1289

Appendix A: Component-wise zodiacal light maps and number density cross-sections

1290

In this Appendix we present maps visualizing of our best-fit ZL model. These figures can help illustrate the physical properties 1291 of the model and help validate how physical our models are. The ZL component-wise maps, both the mission-averaged and the 1292 instantaneous maps in [A.3](#) and [A.2](#), respectively, are compared to the K98 model. 1293

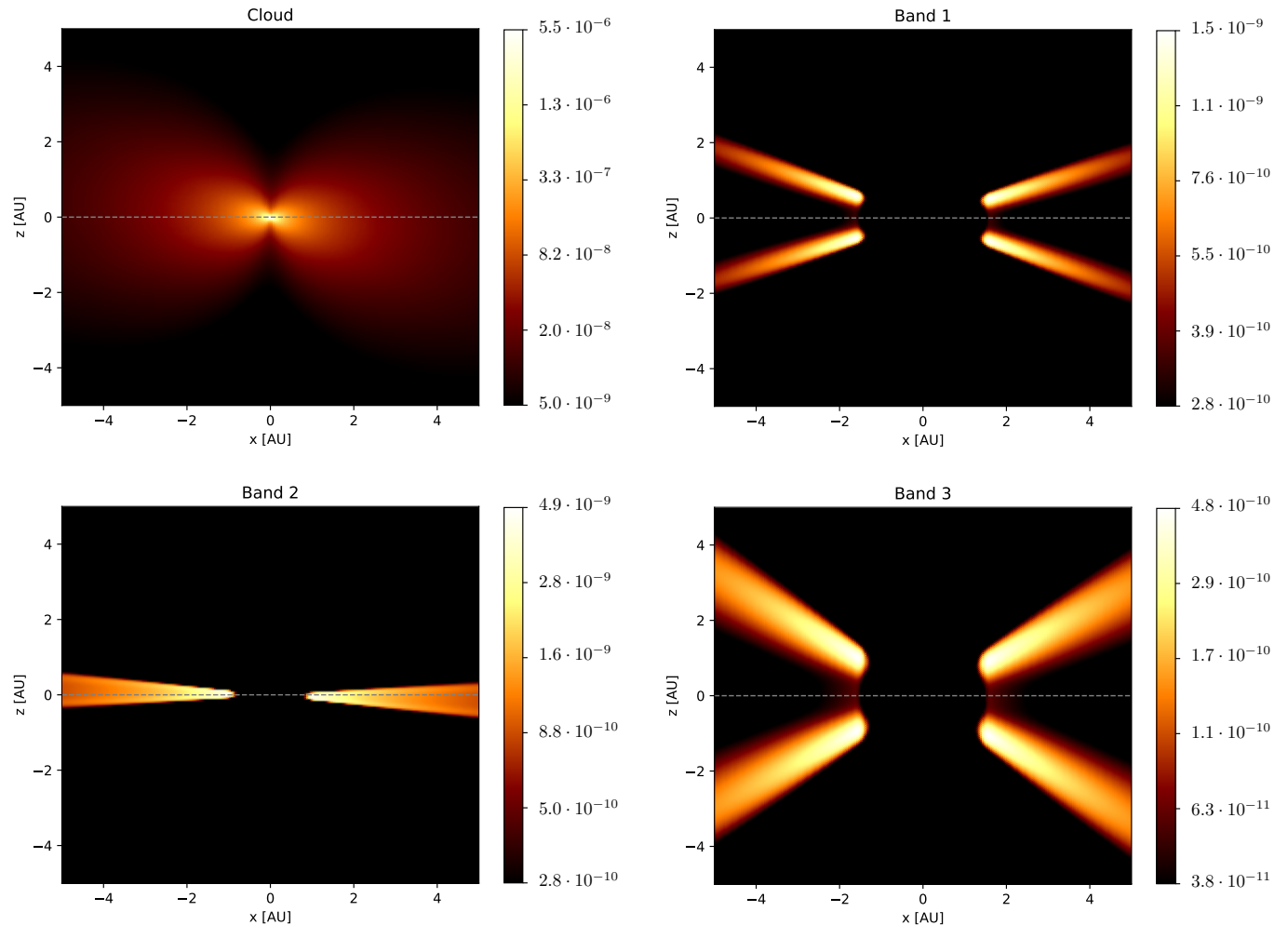


Fig. A.1. Visualization of the IPD number density of the four fitted zodiacal components in our model. The number densities are shown as a cross-section of the Solar system in the xz-plane. (*top left*): The smooth cloud. (*top right*): Dust band 1. (*bottom left*): Dust band 2. (*bottom right*): Dust band 3. The gray dotted line represents the Ecliptic plane and helps illustrate the variations in the components symmetry planes.

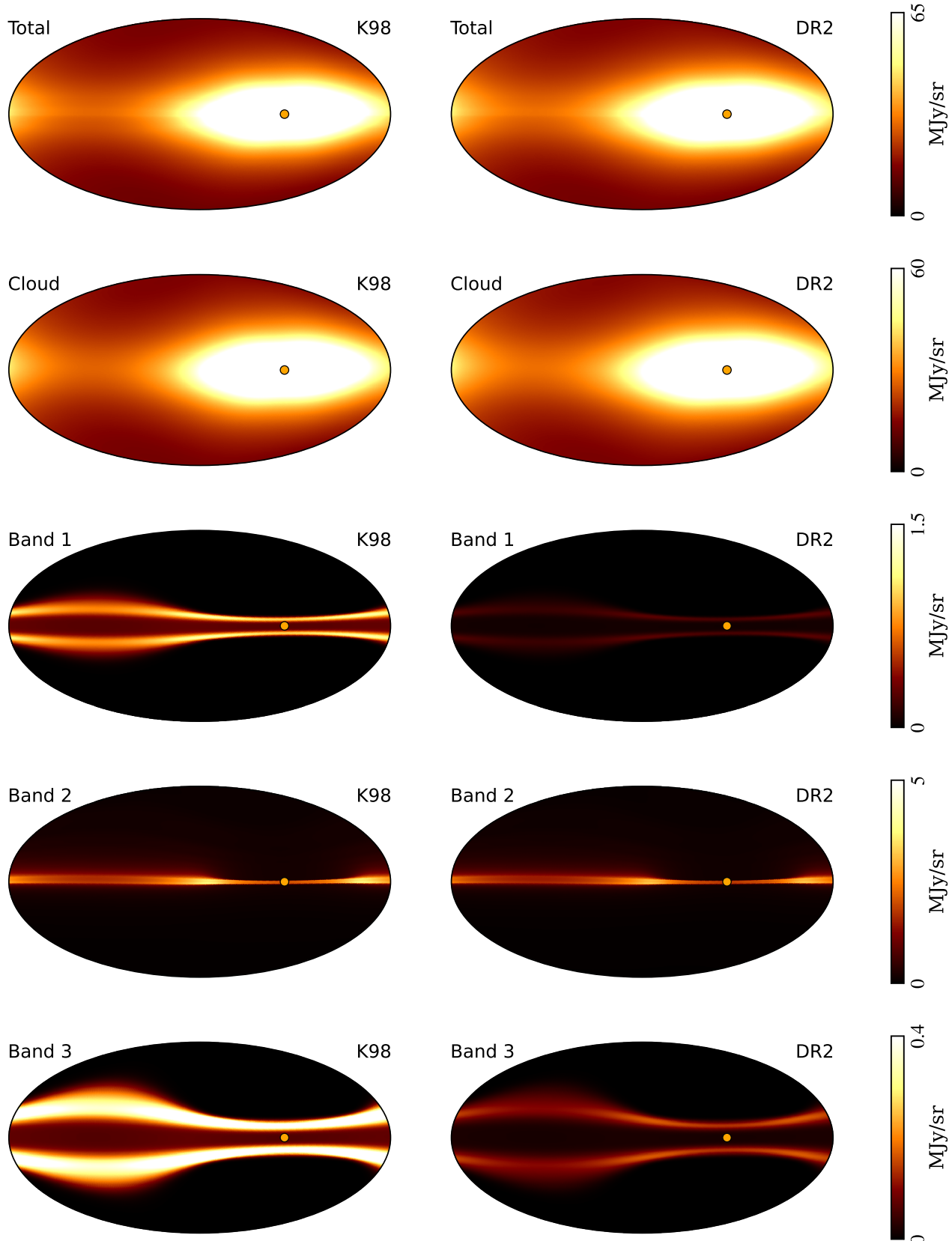


Fig. A.2. Full-sky total and component-wise ZL maps (January 1, 2024) at $25\mu\text{m}$ made with ZodiPy. (*Left column:*) The K98 model. (*Right column:*) Best-fit Cosmoglobe ZL model. Rows list the zodiacal components, from top to bottom, 1) total ZL emission, including the circumstellar ring and Earth-trailing feature; 2) smooth cloud; 3) dust band 1; 4) dust band 2; 5) dust band 3. The maps are in Ecliptic coordinates, with the Sun marked as an orange circle.

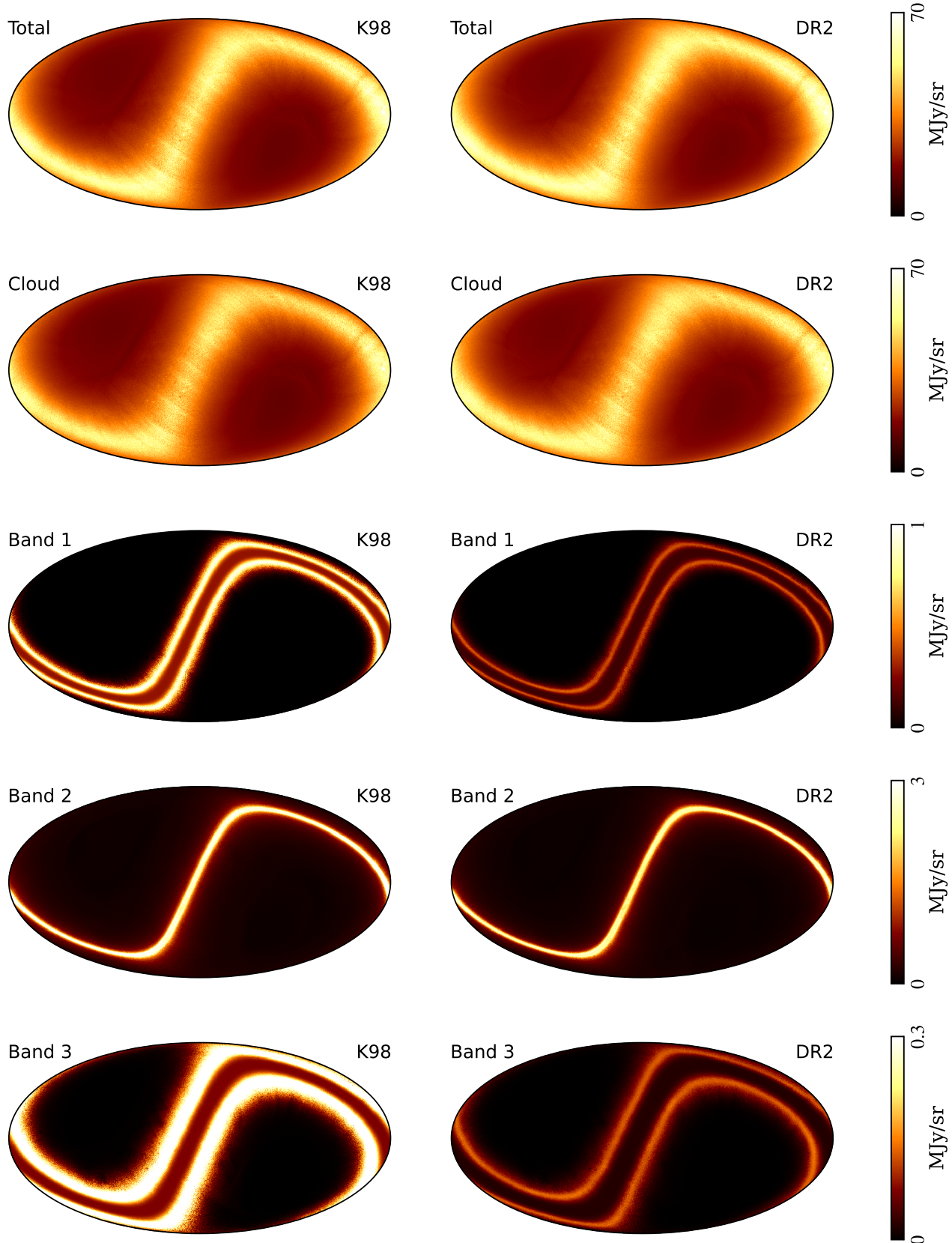


Fig. A.3. Mission-averaged component-wise ZL maps at $25\mu\text{m}$ made with ZodiPy. (*Left column:*) The K98 model. (*Right column:*) Best-fit Cosmoglobe ZL model. Rows list the zodiacal components, from top to bottom, 1) total ZL emission, including the circumsolar ring and Earth-trailing feature; 2) smooth cloud; 3) dust band 1; 4) dust band 2; 5) dust band 3. The maps are in Galactic coordinates.

1294 **Appendix B: Interplanetary dust parameter atlas**

1295 In this Appendix, we present an atlas of mission-averaged ZL parameter maps. Each map represents the effect of changing one ZL
 1296 model parameter by $\pm 5\%$ while holding the other fixed.

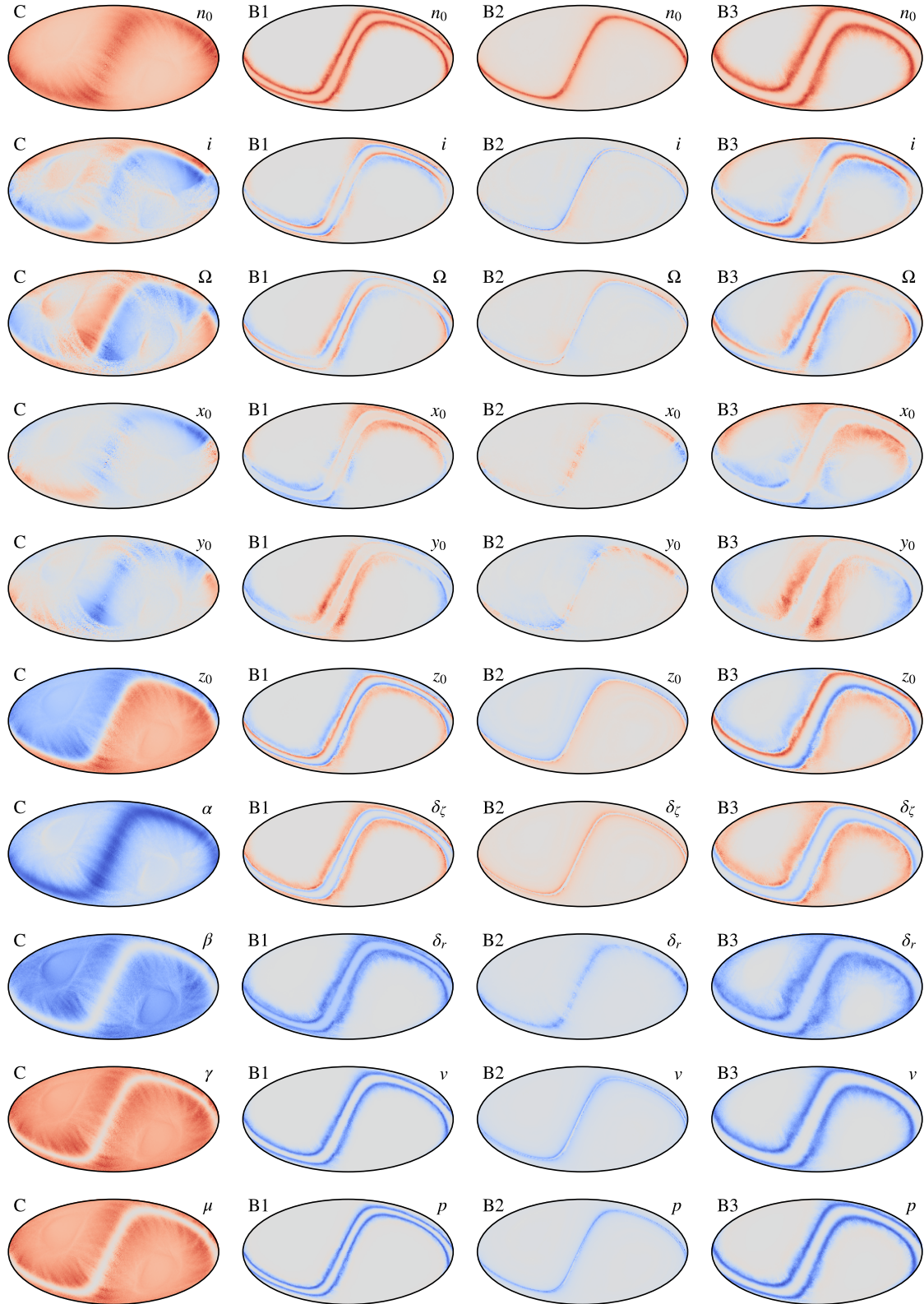


Fig. B.1. ZL parameter atlas showing the difference between increasing and lowering each ZL model parameter by 5% in the form of mission-averaged ZL maps. Columns list, from left to right parameters of 1) the smooth cloud; 2) dust band 1; 3) dust band 2; and 4) dust band 3.

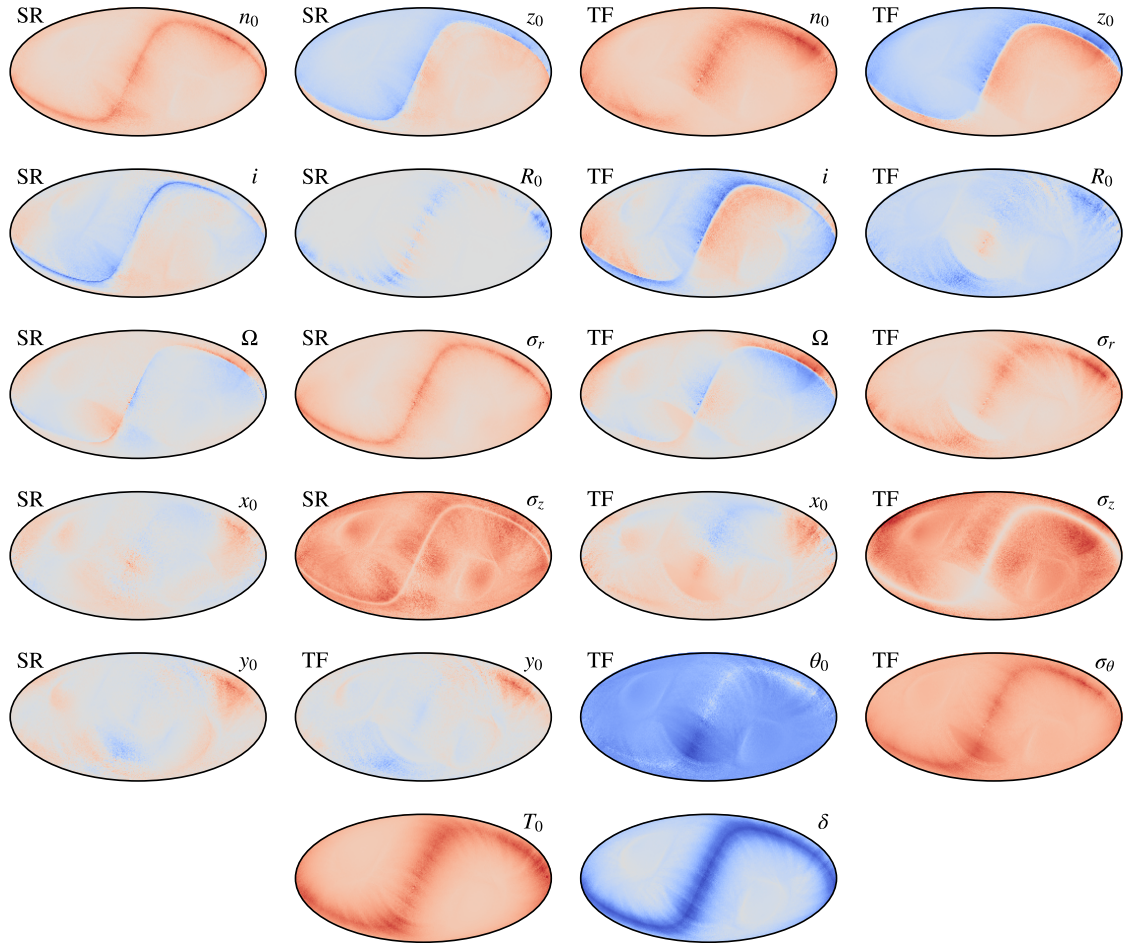


Fig. B.2. ZL parameter atlas showing the difference between increasing and lowering each ZL model parameter by 5% in the form of mission-averaged ZL maps. Columns list the circumsolar ring and Earth-trailing feature components.